ВЗАИМОДЕЙСТВИЯ ИЗЛУЧЕНИЯ И ЧАСТИЦ С КОНДЕНСИРОВАННЫМ ВЕЩЕСТВОМ

Dynamical Theory of Triple-Crystal X-Ray Diffractometry and Characterization of Microdefects and Strains in Imperfect Single Crystals

V. B. Molodkin, S. I. Olikhovskii, E. G. Len, Ye. M. Kyslovskyy,
O. V. Reshetnyk, T. P. Vladimirova, B. V. Sheludchenko, O. S. Skakunova,
V. V. Lizunov, E. V. Kochelab, I. M. Fodchuk[*], and V. P. Klad'ko[**]

*G. V. Kurdyumov Institute for Metal Physics, N.A.S. of Ukraine,
36 Academician Vernadsky Blvd.,
UA-03680 Kyiv, Ukraine*
[*]*Yuriy Fedkovych Chernivtsi National University,
 2 Kotsyubyns'kyy Ave.,
 58012 Chernivtsi, Ukraine*
[**]*V. Ye. Lashkaryov Institute of Semiconductor Physics, N.A.S. of Ukraine,
 41 Nauky Ave.,
 03028 Kyiv, Ukraine*

A short review of basic principles and limitations in obtaining the analytical expressions for the coherent and diffuse scattering intensities measured by the triple-crystal diffractometer (TCD) are presented. Explicit analytical expressions are given for both the diffuse components of TCD profiles and the reciprocal-lattice maps measured within the Bragg diffraction geometry from crystals containing microdefects of several types. These formulas are derived by using the generalized dynamical theory of X-ray scattering by imperfect crystals with randomly distributed microdefects. Some examples demonstrating possibilities of the developed theory for quantitative characterization of structural imperfections in real single crystals are represented. In particular, characteristics of the complicated microdefect structures fabricated in various silicon crystals

Correspondence author: Stepan Iosypovych Olikhovskii
E-mail: olikhovsky@meta.ua

grown by Czochralski technique and floating-zone melting method are determined by analytical treatment of the measured TCD profiles, rocking curves, and reciprocal space maps.

В роботі представлено короткий огляд основних принципів, що використовуються при одержанні аналітичних виразів для когерентної та дифузної інтенсивностей розсіяння, виміряних трикристальним дифрактометром (ТКД). Одержано точні аналітичні вирази для дифузних компонент як ТКД-профілів, так і мап оберненого простору, виміряних у геометрії дифракції за Бреґґом для кристалів, які містять мікродефекти декількох типів. Ці формули одержано при використанні узагальненої динамічної теорії розсіяння Рентґенових променів неідеальними кристалами з випадково розподіленими мікродефектами. Представлено деякі приклади, які демонструють можливості розробленої теорії для кількісної характеризації недосконалостей структури в реальних монокристалах. Зокрема, шляхом аналітичного обробляння виміряних ТКД-профілів, кривих відбивання і мап оберненого простору визначено характеристики складних структур мікродефектів, створених у кристалах силіцію методами Чохральського і зонного топлення.

Ключові слова: динамічне розсіяння, трикристальний дифрактометр, двокристальний дифрактометр, мікродефекти.

В работе представлен краткий обзор основных принципов, используемых при получении аналитических выражений для когерентной и диффузной интенсивностей рассеяния, измеряемых трёхкристальным дифрактометром (ТКД). Получены точные аналитические выражения для диффузных компонент как ТКД-профилей, так и карт обратного пространства, измеренных в геометрии дифракции по Брэггу для кристаллов, содержащих микродефекты нескольких типов. Эти формулы получены при использовании обобщённой динамической теории рассеяния рентгеновских лучей неидеальными кристаллами со случайно распределёнными микродефектами. Представлены некоторые примеры, демонстрирующие возможности разработанной теории для количественной характеризации несовершенств структуры в реальных монокристаллах. В частности, путём аналитической обработки измеренных ТКД-профилей, кривых отражения и карт обратного пространства определены характеристики сложных структур микродефектов, созданных в кристаллах кремния методами Чохральского и зонной плавки.

Ключевые слова: динамическое рассеяние, трёхкристальный дифрактометр, двухкристальный дифрактометр, микродефекты.

1. INTRODUCTION

Modern growth technologies provide producing nearly perfect single

crystals and crystalline devices. The existing level of growth techniques including 'defect engineering' allows for purposeful introducing defects in a crystal lattice to satisfy needs for a wide variety of their mechanical, optical, electric, magnetic properties, *etc*. The nondestructive control of defect structures in such crystal systems is exclusively important to control growth processes. The most informative among different physical characterization methods are the X-ray diffraction techniques; in particular, those based on measurements of diffraction intensity distributions in the reciprocal lattice space by means of the triple-crystal diffractometer (TCD).

The triple-crystal X-ray diffractometry provides the possibilities of very complete and precise characterization of both structural defects in crystal bulk and strains in disturbed surface layers [1−12] as well as chemical compositions and strain distributions in thin film structures, multilayer systems, superlattices, *etc*. [13, 14]. However, at the analysis of TCD measurements, the consideration is usually restricted to the investigation of the diffuse scattering intensity distributions only in those regions where the coherent component of the diffraction intensity can be neglected, or this component can be subtracted by using the equations for perfect crystals. Similarly, the attenuation of coherent scattering intensity due to diffuse scattering from defects is as rule neglected. Such kind approaches can lead to systematic errors when determining the characteristics of crystal structure imperfections.

Strongly speaking, the more rigorous treatment of the diffraction patterns measured by TCD requires the joint consideration of the superimposed coherent and diffuse scattering intensity distributions. This implies also the account for dynamical effects in diffuse scattering intensity and diffuse scattering effects in coherent intensity distributions. Such self-consistent approach in the triple-crystal X-ray diffractometry [15−19], which is necessary for the reliable quantitative characterization of defects and strains in crystals, was consequently developed on the base of the generalized dynamical theory of X-ray scattering by imperfect crystals with randomly distributed microdefects [20−22].

The purpose of this article is reviewing basic principles of the generalized dynamical theory of X-ray diffraction by crystals with chaotically distributed microdefects and the description of corresponding analytical expressions for diffraction profiles and reciprocal lattice maps measured by TCD. Also, the application of these theoretical results on some examples demonstrating possibilities of the developed theory for quantitative characterization of structural imperfections in real single crystals will be represented.

Below, the basic principles of the generalized dynamical theory of X-ray scattering by imperfect single crystals with randomly distributed microdefects will shortly be stated and the analytical expressions for

the differential dynamical coherent and diffuse scattering amplitudes in such crystals will be given in Sect. 2. Various methods of triple-crystal X-ray diffractometry, which are based on this theory, such as reciprocal space mapping, differential-integral method, and separation of coherent and diffuse components of integrated diffraction intensity will be described in Sect. 3. Examples of the quantitative characterization of microdefect structures in various silicon crystals will be given in Sect. 4.

2. DIFFERENTIAL REFLECTIVITY OF SINGLE CRYSTALS WITH MICRODEFECTS

2.1. Basic Assumptions of the Generalized Statistical Dynamical Theory

The polarizability $\chi(\mathbf{r})$ of a crystal with random distribution of defects is a non-periodic function which can be represented as Fourier integral over the whole momentum space. Then, from Maxwell's equations after the Fourier transformation at $|\chi| \ll 1$, the set of basic equations of dynamical theory for the imperfect crystal in momentum space can be derived [21]:

$$(K^2 - k^2)\mathbf{D_k} - \sum_{\mathbf{G}}\sum_{\mathbf{q}} \chi_{\mathbf{G+q}}\mathbf{k} \times \mathbf{k} \times \mathbf{D_{k-G-q}} = \mathbf{0}, \tag{1}$$

where $K = 2\pi/\lambda$ is the modulus of the wave vector $\mathbf{K}$ of the incident plane wave, λ is the X-ray wavelength, $\mathbf{D_q}$ and $\chi_\mathbf{q}$ are Fourier components of electric induction and crystal polarizability, respectively, $\mathbf{G}$ runs over all reciprocal lattice vectors, and $\mathbf{q}$ and $\mathbf{k}$ run over N discrete values in first Brillouin zone (N is the number of crystal lattice points). This set consists of an infinite number of linear algebraic equations for an infinite number of unknown amplitudes of coherent and diffusely scattered plane waves within the crystal.

The set of basic equations (1) is valid only for the homogeneous random distribution of microdefects. Such distribution provides the equivalence of averaging over crystal lattice points and averaging over defect ensemble as well as the translation invariance of the ensemble-averaged polarizability:

$$\left\langle \chi(\mathbf{r} + \mathbf{R}_s^0) \right\rangle = \left\langle \chi(\mathbf{r}) \right\rangle = \sum_{\mathbf{G}} \chi_{\mathbf{G}} \exp(-i\mathbf{Gr}), \tag{2}$$

where corner brackets denote the ensemble averaging, $\mathbf{R}_s^0 = \left\langle \mathbf{R}_s \right\rangle$ are the average lattice vectors (s runs over N lattice points), and $\mathbf{G}$ are the corresponding 2π times reciprocal lattice vectors. Fourier component of polarizability in Eq. (2) is equal to $\chi_{\mathbf{G}} = \chi_{\mathbf{G}}^0 E$, if the changes of struc-

tural factors of unit cells due to static distortions can be neglected. Here, χ_G^0 is the Fourier component of the perfect crystal polarizability and the static Krivoglaz–Debye–Waller factor is defined as $E = \exp(-L_G) = \langle \exp(-i\mathbf{G}\mathbf{u}(\mathbf{R}_s)) \rangle$, where the static displacement field $\mathbf{u}(\mathbf{R}_s) = \mathbf{R}_s - \mathbf{R}_s^0$ can be described at the small concentration of randomly distributed defects $c \ll 1$ by the superposition of static displacements of matrix atoms $\mathbf{U}(\mathbf{r})$, which are caused by a single defect [23]:

$$\mathbf{u}(\mathbf{R}_s) = \sum_t (c_t - c)\,\mathbf{U}(\mathbf{R}_s - \mathbf{R}_t). \tag{3}$$

The random occupation numbers c_t are equal to 1, if the lattice point with radius-vector $\mathbf{R}_t^0$ is occupied by the centre of a microdefect, and 0, if not. The averaging is performed just over these random numbers for which $\langle c_t \rangle = c$.

Thus, the total polarizability of the crystal with randomly distributed microdefects can be represented as the sum of average and fluctuating (random) parts, *i.e.*

$$\chi(\mathbf{r}) = \langle \chi(\mathbf{r}) \rangle + \delta\chi(\mathbf{r}), \tag{4}$$

where $\langle \chi(\mathbf{r}) \rangle$ is described by Eq. (2). Similarly, the wave field in the crystal can be subdivided into average and fluctuating parts:

$$\mathbf{D}(\mathbf{r}) = \langle \mathbf{D}(\mathbf{r}) \rangle + \delta\mathbf{D}(\mathbf{r}), \tag{5}$$

which correspond to coherent and diffusely scattered waves, respectively:

$$\langle \mathbf{D}(\mathbf{r}) \rangle = e^{-i\mathbf{K}_0\mathbf{r}} \sum_G \mathbf{D}_G\, e^{-i\mathbf{G}\mathbf{r}}, \tag{6}$$

$$\delta\mathbf{D}(\mathbf{r}) = e^{-i\mathbf{K}_0\mathbf{r}} \sum_G \sum_{q \neq 0} \mathbf{D}_{G+q}\, e^{-i(\mathbf{G}+\mathbf{q})\mathbf{r}}, \tag{7}$$

where the constant wave vector $\mathbf{K}_0$ of the transmitted coherent plane wave in crystal has been introduced for the sake of convenience in subsequent consideration.

In the two-beam case of diffraction, only two so-called strong Bragg (coherent) waves are excited in the crystal and, consequently, in Eqs. (1) as well as in Eqs. (6) and (7) only two amplitudes of coherent waves ($\mathbf{D}_G$) and corresponding $2N$ amplitudes of diffusely scattered waves ($\mathbf{D}_{G+q}$) with $\mathbf{G} = 0$ and $\mathbf{H}$ should be retained, whereas the rest of amplitudes of (weak) Bragg and diffusely scattered waves can be neglected. The infinite equations set (1) can be represented then for each of two (σ and π) polarization states as two equation sets, namely, one for two amplitudes of coherent transmitted (D_0) and diffracted (D_H) plane

waves with wave vectors $\mathbf{k} = \mathbf{K}_0$ and $\mathbf{k} = \mathbf{K}_H = \mathbf{K}_0 + \mathbf{H}$, respectively, and another one for $2N$ amplitudes of transmitted ($D_\mathbf{q}$) and diffracted ($D_{\mathbf{H}+\mathbf{q}}$) diffuse plane waves with wave vectors $\mathbf{k} = \mathbf{K}_{0\mathbf{q}} = \mathbf{K}_0 + \mathbf{q}$ and $\mathbf{k} = \mathbf{K}_{H\mathbf{q}} = \mathbf{K}_H + \mathbf{q}$, respectively.

These sets of coupled equations can be decoupled and solved by using the perturbation theory. [21, 22] if inequalities hold for the dispersion corrections to the wave vectors of coherent and diffusely scattered waves, respectively, which describe the attenuation of these waves due to diffuse scattering:

$$\left|\Delta\chi_{\mathbf{GG}'}(\Delta\theta)\right| \ll E\left|\chi_{\pm\mathbf{H}}\right|, \quad \left|\Delta\chi'_{\mathbf{GG}}(\Delta\theta, \Delta\theta')\right| \ll E\left|\chi_{\pm\mathbf{H}}\right|, \tag{8}$$

where dispersion corrections are defined as quadratic combinations of Fourier components of the fluctuating part of crystal polarizability, $\Delta\theta$ and $\Delta\theta'$ are the angular deviations of the wave vectors of coherent and diffusely scattered waves from their exact Bragg conditions, $\mathbf{G}$ and $\mathbf{G}' = \mathbf{0}$ or $\mathbf{H}$.

The dispersion corrections to the wave vectors of coherent and diffusely scattered waves describe the dynamical effects of influence of the elastic diffuse scattering from defects through virtual ($P_{\mathbf{GG}'}^{\delta}, P_{\mathbf{GG}'}'^{\delta\tau}$) and energy-conserved ($\mu_{\mathbf{GG}'}^{\delta}, \mu_{\mathbf{GG}'}'^{\delta\tau}$) scattering channels on the angular redistribution and attenuation of the coherent and diffusely scattered intensity, respectively:

$$\Delta\chi_{\mathbf{GG}'}^{\delta}(\Delta\theta) = P_{\mathbf{GG}'}^{\delta}(\Delta\theta) - i\mu_{\mathbf{GG}'}^{\delta}(\Delta\theta) / K, \tag{9}$$

$$\Delta\chi_{\mathbf{GG}'}'^{\delta\tau}(\Delta\theta, \Delta\theta') = P_{\mathbf{GG}'}'^{\delta\tau}(\Delta\theta, \Delta\theta') - i\mu_{\mathbf{GG}'}'^{\delta\tau}(\Delta\theta, \Delta\theta') / K, \tag{10}$$

where δ and $\tau = 1, 2$ numerate coherent and diffuse wave fields, respectively, and the quantities $P_{\mathbf{GG}'}^{\delta}$ ($P_{\mathbf{GG}'}'^{\delta\tau}$) and $\mu_{\mathbf{GG}'}^{\delta}$ ($\mu_{\mathbf{GG}'}'^{\delta\tau}$) are of the same order of magnitude.

In the derivation of compact analytical expressions for the diffuse scattering intensity, the inequalities were taken into account:

$$\left|\left\langle \delta\chi_\mathbf{q}\delta\chi_{-\mathbf{q}} \right\rangle\right| \ll \left|\left\langle \delta\chi_\mathbf{q}\delta\chi_{-\mathbf{q}\pm\mathbf{H}} \right\rangle\right| \ll \left|\left\langle \delta\chi_{\mathbf{q}\pm\mathbf{H}}\delta\chi_{-\mathbf{q}\pm\mathbf{H}} \right\rangle\right|, \tag{11}$$

where $\delta\chi_{\mathbf{G}+\mathbf{H}}$ ($\mathbf{G} = \mathbf{0}, \pm\mathbf{H}$) are fluctuating Fourier components of crystal polarizability. These inequalities are valid for typical microdefects at sufficiently small $q \ll H$.

2.2. Differential Reflectivity of Imperfect Single Crystals

The differential intensity of X-ray scattering by the imperfect single crystal containing homogeneously distributed microdefects can be represented as the sum of coherent or Bragg (R_B) and diffuse (R_D) compo-

nents (see Refs. [20−22]):

$$R_{\rm S}({\bf k}) = R_{\rm B}({\bf k}) + R_{\rm D}({\bf k}), \qquad (12)$$

where ${\bf k} = {\bf K}' - {\bf K} - {\bf H}$ is the deviation of the wave vector ${\bf K}'$ of the scattered plane wave from the reciprocal lattice point H, which corresponds to the reciprocal lattice vector ${\bf H}$, and ${\bf K}$ is the wave vector of the incident plane wave.

The coherent component of the crystal reflectivity has the form

$$R_{\rm B}({\bf k}) = R_{\rm coh}(\Delta\theta, \varphi)\delta(\Delta\theta' - b\Delta\theta)\delta(\varphi' - \varphi), \qquad (13)$$

$$R_{\rm coh}(\Delta\theta) = \left| r(\Delta\theta) \right|^2, \qquad (14)$$

where $\delta(x)$ is Dirac's δ-function, $\Delta\theta$ and $\Delta\theta'$ are the angular deviations of the wave vectors of incident and scattered plane waves in the horizontal plane from the directions satisfying exactly the Bragg condition, $b = \gamma_0|\gamma_{\rm H}|^{-1}$ is the parameter of diffraction asymmetry, $\gamma_0 = \sin(\theta_{\rm B} - \psi)$ and $\gamma_{\rm H} = -\sin(\theta_{\rm B} + \psi)$ are direction cosines relatively to the inner normal n to the entrance crystal surface for wave vectors ${\bf K}$ and ${\bf K}'$, respectively, ψ is the angle between surface and reflecting planes of the crystal, $\theta_{\rm B}$ is the Bragg angle, φ and φ' are the angular deviations of the wave vectors ${\bf K}$ and ${\bf K}'$ from the horizontal plane, respectively.

2.2.1. Coherent Component of Reflectivity of Imperfect Crystal

According to the generalized dynamical theory of the X-ray scattering in imperfect single crystals [21, 22], the amplitude reflection coefficient in Eq. (14) can be written for each polarization state (σ and π) in the form:

$$r(\Delta\theta) = \sqrt{\zeta}\left[y + i\sqrt{y^2 - 1}\,{\rm ctg}(A\sqrt{y^2 - 1}) \right]^{-1}, \qquad (15)$$

where the notation was used:

$$A = \pi t/\Lambda, \quad \Lambda = \lambda\sqrt{\gamma_0\,|\gamma_{\rm H}|}/\sigma, \qquad (16)$$

$$\zeta = (CE\chi_{\rm H} + \Delta\chi_{\rm H0})(CE\chi_{\rm -H} + \Delta\chi_{\rm 0H})^{-1}, \quad \sigma^2 = (CE\chi_{\rm H} + \Delta\chi_{\rm H0})(CE\chi_{\rm -H} + \Delta\chi_{\rm 0H}),$$

with t and Λ being the crystal thickness and extinction length, respectively, and C is the polarization factor equal to 1 or $\cos(2\theta_{\rm B})$ for σ- and π-polarization states, respectively. The normalized angular deviation of the crystal is defined as

$$y = (\alpha - \alpha_0)\sqrt{b}/\sigma, \quad \alpha = -\Delta\theta\sin(2\theta_{\rm B}), \qquad (17)$$

$$2\alpha_0 = \chi_0 + \Delta\chi_{HH} + (\chi_0 + \Delta\chi_{00}) / b.$$

In the limiting case of the thick crystal, *i.e.*, when $\mu_0 t \gg 1$, where μ_0 is the linear coefficient of photoelectric absorption, Eq. (15) can be simplified to the form:

$$r(\Delta\theta) = \zeta^{-1/2}(y - s\sqrt{y^2 - 1}), \tag{18}$$

where $s = \mathrm{sgn}(y_r)$, $y_r = \mathrm{Re}(y)$.

It should be remarked that the dispersion corrections to the wave vectors of coherent and diffusely scattered waves, which appeared in Eq. (15) to (18) and describe the attenuation of these waves due to diffuse scattering, are connected immediately with the coefficient of absorption due to diffuse scattering, $\mu_{ds}(\Delta\theta)$:

$$\mu_{HH}^{\delta}(\Delta\theta) \approx \mu_{ds}(\Delta\theta), \quad \mu_{00}^{\delta}(\Delta\theta) \approx -b\mu_{HH}^{\delta}(\Delta\theta), \tag{19}$$
$$P_{HH}^{\delta}(\Delta\theta) \approx -K^{-1}\mu_{HH}^{\delta}(\Delta\theta), \quad P_{00}^{\delta}(\Delta\theta) \approx -bP_{HH}^{\delta}(\Delta\theta).$$

In turn, this coefficient is related to the correlation function $S(\mathbf{q})$ describing the differential distribution of diffusely scattered waves:

$$\mu_{ds}(\Delta\theta) = \frac{C^2 V}{4\lambda^2} \int d\mathbf{k}' S(\mathbf{q}), \tag{20}$$

where the integration is performed over the plane tangent to Ewald sphere near the reciprocal lattice point considered. The correlation function in Eq. (20) is defined as follows:

$$S(\mathbf{q}) = \mathrm{Re}\left\langle \delta\chi_{\mathbf{q}+\mathbf{H}}\delta\chi_{-\mathbf{q}-\mathbf{H}} \right\rangle, \tag{21}$$

where $\mathbf{q} = \mathbf{k} + i\mu_i\mathbf{n}$, and μ_i is the limiting value of an interference absorption coefficient at $|\Delta\theta|$ and $|\Delta\theta'| \to \infty$.

It should also be noted that the non-diagonal dispersion corrections to the wave vectors of coherent waves can be neglected for typical microdefects with radii significantly smaller than extinction length:

$$P_{0H}^{\delta}(\Delta\theta) \approx P_{H0}^{\delta}(\Delta\theta) \approx 0, \quad \mu_{0H}(\Delta\theta) \approx \mu_{H0}(\Delta\theta) \approx 0. \tag{22}$$

The relations for the dispersion corrections to the wave vectors of diffusely scattered waves are similar to those described above in Eqs. (19) to (22) for the dispersion corrections to the wave vectors of coherent waves.

Thus, the complex dispersion corrections due to diffuse scattering and static Krivoglaz–Debye–Waller factor do account for diffuse scattering effects in the coherent component of the crystal reflectivity and

establish its relation to defect characteristics.

2.2.2. Influence of Distorted Thin Surface Layer

Disturbed or distorted surface layers often are present in crystals with strains caused by artificial modification [3, 5, 23] or natural relaxation, particularly, due to 'mirror image forces' from point defects [24, 25] and microdefects [20, 26]. The coherent component of amplitude reflectivity of an imperfect crystal with defects and disturbed surface layer can be found from the reduced Takagi–Taupin equation for the case of an arbitrary (but not fluctuating) one-dimensional strain field [18]:

$$-i\frac{dX}{dZ} = X^2 - 2\eta X + 1, \tag{23}$$

$$X(z) = (\zeta b)^{-1/2} D_{\mathrm{H}}/D_0, \quad Z = \pi(z - d)/\Lambda, \tag{24}$$

with the boundary condition $X(d) = X_0$, where d is the layer thickness and $z = 0$ corresponds to the crystal surface. The equation (23) should be modified by renormalizing variables and replacing diffraction parameters for perfect crystal by those for imperfect crystal with defects to account for the presence of randomly distributed Coulomb-type defects in the layer and substrate, namely:

$$\eta = y + y_{\mathrm{S}}, \quad y_{\mathrm{S}} = \alpha_{\mathrm{S}}\sqrt{b}/\sigma, \quad \alpha_{\mathrm{S}} = -\Delta\omega\sin(2\theta_{\mathrm{B}}), \tag{25}$$

$$\Delta\omega = (\varepsilon_\perp \cos^2\psi + \varepsilon_{||}\sin^2\psi)\tan\theta_{\mathrm{B}} + (\varepsilon_\perp - \varepsilon_{||})\sin\psi\cos\psi\,\mathrm{sgn}(1-b), \tag{26}$$

where $\varepsilon_\perp$ and $\varepsilon_{||}$ are normal and parallel strain components, respectively.

The corresponding boundary condition has the form:

$$X(d) = X_0 = \zeta^{-1/2}r(\Delta\theta), \tag{27}$$

where the amplitude reflectivity of substrate is described by Eq. (15).

For the sufficiently thin disturbed surface layer whose thickness is significantly smaller as compared with extinction length, i.e., $d \ll \mathrm{Re}(\Lambda)$, the dynamical effects of coherent scattering can be neglected and corresponding quadratic term in the Takagi–Taupin equation (15) can be dropped:

$$i\frac{dX}{dZ} = 2\eta X - 1. \tag{28}$$

Then, the coherent component of amplitude reflectivity of the imper-

fect crystal with defects and disturbed surface layer with constant strain can be found in kinematical approximation:

$$X(z) = X_0 e^{-2i\eta Z} + \frac{1 - e^{-2i\eta Z}}{2\eta}. \qquad (29)$$

It is obvious that representation of the strain in disturbed layer by one-step profile is rather a rough model. More realistic is the model presented by the multi-step strain profile which corresponds to so-called 'layer approximation'. For the multilayer structure with constant average strain ε^i in each layer of thickness t_i, the solution of Eq. (28) can be easily found by iteration. The iteration procedure is performed by using the solution (29) for the first layer adjacent to the substrate as the boundary condition for equation in the second layer, *etc.*

As result, we obtain the coherent component of reflectivity of the imperfect crystal with defects and inhomogeneous disturbed surface layer:

$$R_{\text{coh}} = |\zeta| |X(0)|^2 = R_{\text{coh}}^0 + R_{\text{coh}}^{\text{int}} + R_{\text{coh}}^{\text{kin}}, \qquad (30)$$

$$R_{\text{coh}}^0 = |\zeta| |X_0|^2 \exp(-2 \operatorname{Im} \varphi_0), \qquad (31)$$

$$R_{\text{coh}}^{\text{int}} = 2|\zeta| \operatorname{Re} \left[X_{\text{kin}}^* X_0 \exp(i\varphi_0) \right], \qquad (32)$$

$$R_{\text{coh}}^{\text{kin}} = |\zeta| |X_{\text{kin}}|^2, \qquad (33)$$

$$X_{\text{kin}} = \sum_{j=1}^N e^{i\varphi_j} \frac{1 - \exp(2i\eta_j T_j)}{2\eta_j},$$

where the notation was used (N is the number of sublayers in the disturbed layer):

$$\varphi_j = 2 \sum_{i=j+1}^N \eta_i T_i, \ j = 0, N - 1, \ \varphi_N = 0, \ T_i = \pi t_i / \Lambda, \qquad (34)$$

$$\eta_i = y + y_S^i, \ y_S^i = \alpha_S^i \sqrt{b} / \sigma, \ \alpha_S^i = -\Delta\omega_i \sin(2\theta_B), \qquad (35)$$

$$\Delta\omega_i = (\varepsilon_\perp^i \cos^2 \psi + \varepsilon_{||}^i \sin \psi) \tan \theta_B + (\varepsilon_\perp^i - \varepsilon_{||}^i) \sin \psi \cos \psi \operatorname{sgn}(1 - b). \quad (36)$$

It should be emphasized that Eqs. (30) to (36) for the coherent component of reflectivity of the imperfect crystal with defects and inhomogeneous disturbed surface layer provide the possibility for accounting the influence of not only randomly distributed microdefects in crystal bulk but also subsurface strains caused by artificial modification or natural relaxation, particularly, due to 'mirror image forces' from point defects.

2.2.3. Diffuse Component of Imperfect Crystal Reflectivity

The diffuse component of the dynamical differential reflection coefficient of imperfect crystal with randomly distributed microdefects has the form [22]:

$$R_{\mathrm{D}}(\mathbf{k}) = \frac{\left\langle \left| f_{\mathrm{H}}\left(\mathbf{K}', \mathbf{K}\right) \right|^2 \right\rangle}{\gamma_0 S \left| E_0 \right|^2}, \tag{37}$$

where $f_{\mathrm{H}}(\mathbf{K}', \mathbf{K})$ is the diffuse scattering amplitude, and S is the illuminated area of the entrance crystal surface, E_0 is the amplitudes of incident plane wave in vacuum. The diffuse scattering amplitude in Eq. (37) is formed by contributions from partial diffuse scattering amplitudes $F_{\mathrm{HG}}^{\delta}(\mathbf{K}', \mathbf{K})$ describing the scattering of coherent waves $D_{\mathrm{G}}^{\delta}(\mathbf{K})$ into diffuse ones:

$$f_{\mathrm{H}}(\mathbf{K}', \mathbf{K}) = \sum_{\delta} \sum_{\mathbf{G}} D_{\mathrm{G}}^{\delta}(\mathbf{K}) F_{\mathrm{HG}}^{\delta}(\mathbf{K}', \mathbf{K}), \tag{38}$$

where $\delta = 1, 2$ and $\mathbf{G} = \mathbf{0}, \mathbf{H}$.

In the limiting case of the thick crystal, the expression (37) can be reduced to the form:

$$R_{\mathrm{D}}(\mathbf{k}) \approx \frac{1}{\gamma_0 S} \left(\frac{CVK^2}{4\pi} \right)^2 F_{\mathrm{dyn}} \left\langle \left| \delta\chi_{\mathbf{H}+\mathbf{q}} \right|^2 \right\rangle, \tag{39}$$

where V is the crystal volume, the factor F_{dyn} describes the modulation of diffuse scattering intensity caused by the dynamical interference of strong Bragg waves, $\delta\chi_{\mathbf{H}+\mathbf{q}}$ is the Fourier component of the fluctuation part of the crystal polarizability, and the interference absorption coefficient μ_i in the complex momentum transfer $\mathbf{q} = \mathbf{k} + i\mu_i\mathbf{n}$ describes the extinction effect for diffusely scattered waves.

The diffuse component of the differential crystal reflectivity can be written after averaging over random distribution of defects as follows:

$$R_{\mathrm{D}}(\mathbf{k}) = \pi^{-1} M K^2 F(\mathbf{q}), \tag{40}$$

$$M = c m_0 C^2 E^2 p(t) / \gamma_0, \quad m_0 = \pi v_{\mathrm{c}} (H |\chi_{\mathbf{H}}| / \lambda)^2 / 4,$$

$$p(t) = \left[1 - \exp(-2\mu_i t) \right] \left(2\mu_i t \right)^{-1},$$

where c is the concentration of randomly distributed microdefects per one lattice site, v_{c} is the unit cell volume, and t is the crystal thickness.

Function $F(\mathbf{q})$ in Eq. (40) for momentum transfers in Huang scattering region, *i.e.*, at $k \ll k_{\mathrm{m}} = 1/R_{\mathrm{eff}}$, where R_{eff} is an effective radius of defect [22], can approximately be written in the form:

$$F(\mathbf{q}) = F^{\mathrm{H}}(\mathbf{q}) = H^2 \left(B_1 + B_2 \frac{|\mathbf{H}_0\mathbf{q}|^2}{|\mathbf{q}|^4} \right) \frac{1}{|\mathbf{q}|^2} + HB_3 \frac{1}{|\mathbf{q}|}, \qquad (41)$$

where the effective radii of defects are defined as $R_{\mathrm{eff}} = E(HA_{\mathrm{C}})^{1/2}$ and $R_{\mathrm{eff}} = ER_{\mathrm{L}}(H\,|\mathbf{b}|)^{1/2}$ for clusters and dislocation loops, respectively, A_{C} is the cluster strength, $\mathbf{b}$ is the Burgers vector, R_{L} is the dislocation loop radius, and $\mathbf{H}_0 = \mathbf{H}/H$ is a unit vector. Constants B_1 and B_2 are defined for spherical clusters as follow:

$$B_1 = 0,\ B_2 = (4\pi A_{\mathrm{C}}/\upsilon_{\mathrm{c}})^2,\ A_{\mathrm{C}} = \Gamma\varepsilon R_{\mathrm{C}}^3,\ \Gamma = (1+\nu)(1-\nu)^{-1}/3, \qquad (42)$$

where ε is the strain at cluster boundary, R_{C} is the cluster radius, ν is the Poisson ratio. For circular dislocation loops, the definitions are following:

$$B_1 = \frac{4}{15}(\pi\,|\mathbf{b}|\,R_{\mathrm{L}}^2 / \upsilon_{\mathrm{c}})^2,\ B_2 = \beta B_1,\ \beta = \frac{1}{4}(3\nu^2 + 6\nu - 1)/(1-\nu)^2. \qquad (43)$$

The constant B_3 in Eq. (41) can be put equal to $B_3 = 2L_{\mathrm{H}}B^{1/2}/c$, where for clusters $B = B_2$ and for dislocation loops $B = B_1$.

  For the Stockes–Wilson scattering region ($k \gg k_{\mathrm{m}}$), the function $F(\mathbf{q})$ should be rewritten as follows [22]:

$$F(\mathbf{q}) = F^{\mathrm{S-W}}(\mathbf{q}) = F^{\mathrm{H}}(\mathbf{q})(k_{\mathrm{m}}^2 + \mu_{\mathrm{i}}^{\,2})/(k^2 + \mu_{\mathrm{i}}^{\,2}), \qquad (44)$$

where the antisymmetric term with B_3 coefficient from Eq. (41) should be dropped.

  The expressions (40) to (44) for the diffuse component of reflectivity are valid at arbitrary radii of microdefects (up to the extinction length and larger) and in the whole angular range including the total reflection range due to the account for multiple diffuse scattering processes. Also, these expressions can be used with some precautions to describe contributions from thermal diffuse scattering and diffuse scattering from point defects (see, *e.g.*, Refs. [27, 28]).

3. METHODS OF TRIPLE-CRYSTAL X-RAY DIFFRACTOMETRY

3.1. Reciprocal Space Mapping

3.1.1. Coherent Component of Reciprocal Space Map

The X-ray diffraction intensity from imperfect crystal with defects, which is registered by TCD detector, is the sum of coherent and diffuse components; both reflected from third crystal-analyser and integrated

over horizontal and vertical divergence [15−19]:

$$I(\Delta\theta, \Delta\theta') = I_{\text{coh}}(\Delta\theta, \Delta\theta') + I_{\text{diff}}(\Delta\theta, \Delta\theta'). \tag{45}$$

This intensity depends only on two angular variables, namely, the angular deviations of investigated crystal ($\Delta\theta$) and analyser-crystal ($\Delta\theta'$) from their exact reflecting positions (Fig. 1).

In the case of quasi-non-dispersive geometry ($m, -n, m$) of the optical scheme used conventionally, the coherent component of the intensity measured by TCD can be represented in the form [18]:

$$I_{\text{coh}}(\Delta\theta, \Delta\theta') = I_0 \int\limits_{-\infty}^{\infty} dx R_{\text{M}}\{b_{\text{M}}^{-1}[b_{\text{S}}^{-1}(x - \Delta\theta) - \Delta\theta]\} R_{\text{coh}}[b_{\text{S}}^{-1}(x - \Delta\theta)] R_{\text{A}}(x - \Delta\theta'), \tag{46}$$

where I_0 is the incident X-ray intensity, R_{M} and R_{A} are reflection coefficients of flat or grooved monochromator and analyser crystals, b_{M} and b_{S} are asymmetry parameters of monochromator and investigated crystal, respectively. If structural defects are present in monochromator and analyser crystals, their reflection coefficients also consist of coherent and diffuse components similarly to that of the investigated crystal:

$$R_{\text{M,A}}(x) = R_{\text{coh}}^{\text{M,A}}(x) + R_{\text{diff}}^{\text{M,A}}(x), \tag{47}$$
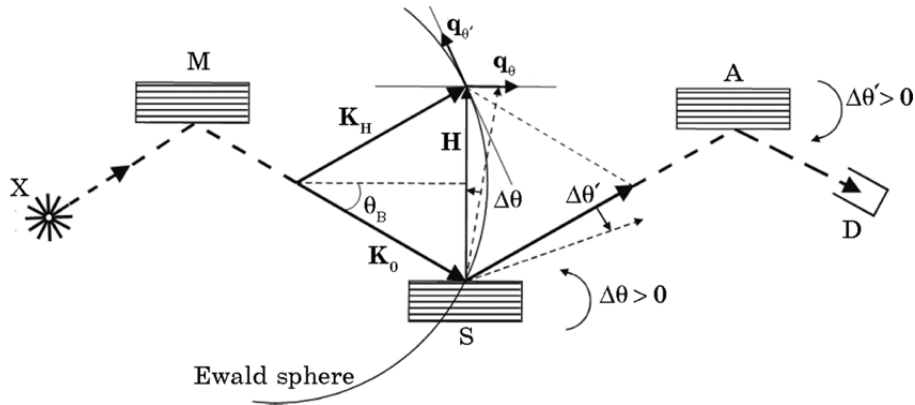

Fig. 1. Scheme applied for mapping the coherent and diffuse scattering intensity distributions in reciprocal space by using TCD measurements at Bragg diffraction geometry. The notation: X—X-ray tube, M—monochromator, S—investigated crystal, A—analyser, D—detector, $\mathbf{K_0}$ and $\mathbf{K_H}$—wave vectors of incident and diffracted waves, respectively, $\mathbf{H}$—reciprocal lattice vector, $\Delta\theta$ and $\Delta\theta'$—angular deviations of S and A crystals from their exact reflecting positions, respectively, $\mathbf{q}_\theta$ and $\mathbf{q}_{\theta'}$—orts of the oblique coordinate system [29].

where diffuse components of reflection coefficients R_M and R_A are described by expressions like Eq. (40). When the multiple reflections are used in monochromator and analyser crystals (Fig. 2), the diffuse components of monochromator and analyser reflection coefficients are strongly suppressed and can be neglected. However, in the case of flat monochromator and analyser crystals these diffuse components can substantially modify observed diffraction patterns [15−17, 30, 31].

3.1.2. Diffuse Component of Reciprocal Space Map

The diffuse component of the diffraction intensity measured by TCD can be represented in the form [19, 32]:

$$I_{\text{diff}}(\Delta\theta, \Delta\theta') = I_0 \int\limits_{-\infty}^{\infty} dx R_M(x) \int\limits_{-\infty}^{\infty} dx' r_{\text{diff}}(\kappa) R_A(x' - \Delta\theta'), \qquad (48)$$

where the function r_{diff} represents the diffuse component of differential reflection coefficient (40) integrated over a vertical divergence:

$$r_{\text{diff}}(\kappa) = K^{-1} \int dk_y R_D(\mathbf{k}). \qquad (49)$$

Here, $\mathbf{k} = \kappa + k_y \mathbf{e_y}$, components k_x and k_z of the vector $\kappa = k_x \mathbf{e_x} + k_z \mathbf{e_z}$ lie in the coherent scattering plane $(\mathbf{K, H})$, $\mathbf{e_y}$ is a normal to this plane, $\mathbf{e_z} \equiv \mathbf{n}$, and components k_x and k_y lie in the crystal surface.

The components k_x and k_z are connected by simple relationships with angular deviations of wave vectors of incident (x) and scattered (x') plane waves from their exact Bragg directions in the scattering plane. In the case of the asymmetric Bragg diffraction geometry these relationships have the form:
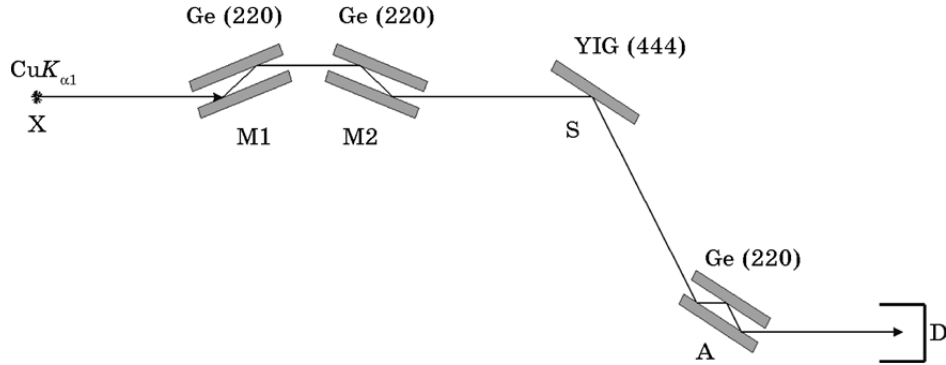

Fig. 2. Scheme used in the typical TCD with the multiple reflections in grooved monochromator (M1, M2) and analyser (A) crystals at Bragg diffraction geometry on the investigated crystal (S) [32].

$$k_x = -K(x + x')\sin(\theta_B + \psi) + 2K(\Delta\theta + x)\sin\theta_B\cos\psi,$$
$$k_z = -K(x + x')\cos(\theta_B + \psi) - 2K(\Delta\theta + x)\sin\theta_B\sin\psi. \quad (50)$$

If the half-width of the function r_{diff} is much larger as compared with half-widths of reflection coefficients of monochromator and analyser crystals, the functions R_M and R_A in Eq. (48) can be replaced by δ-functions:

$$I_{\text{diff}}(\Delta\theta, \ \Delta\theta') \approx I_0 R_{iM} R_{iA} r_{\text{diff}}(k_x, k_z), \quad (51)$$

where R_{iM} and R_{iA} are integrated reflectivities of monochromator and analyser crystals, and components k_x and k_z are described by expressions:

$$k_x = -K\Delta\theta'\sin(\theta_B + \psi) + 2K\,\Delta\theta\sin\theta_B\cos\psi,$$
$$k_z = -K\Delta\theta'\cos(\theta_B + \psi) - 2K\,\Delta\theta\sin\theta_B\sin\psi. \quad (52)$$

Now, after integrating in Eq. (49) over vertical divergence, the diffuse component of the reciprocal space map for imperfect crystals with randomly distributed microdefects can be represented in the Huang scattering region ($\kappa \le k_m$) as follows:

$$r_{\text{diff}}(\kappa) = M[A_H(\kappa) + A_{S-W}(\kappa) + A_a(\kappa)], \quad (53)$$

$$A_H(\kappa) = \frac{K}{\pi\sqrt{\kappa^2 + \mu_i^2}}(2B_1 + B_2 a_\kappa)\arctan\frac{\sqrt{k_m^2 - \kappa^2}}{\sqrt{\kappa^2 + \mu_i^2}}, \quad a_\kappa = \frac{(\mathbf{H}_0\kappa)^2}{\kappa^2 + \mu_i^2}, \quad (54)$$

$$A_{S-W}(\kappa) = \frac{K}{\pi\sqrt{\kappa^2 + \mu_i^2}}\left(B_1 + \frac{3}{4}B_2 a_\kappa\right) \times$$

$$\times\left[\left(\frac{\pi}{2} - \arctan\frac{\sqrt{k_m^2 - \kappa^2}}{\kappa^2 + \mu_i^2}\right)\frac{k_m^2 + \mu_i^2}{\kappa^2 + \mu_i^2} - \frac{\sqrt{k_m^2 - \kappa^2}}{\sqrt{\kappa^2 + \mu_i^2}}\right] + B_2 a_\kappa \frac{K}{2\pi}\frac{\sqrt{k_m^2 - \kappa^2}}{\sqrt{\kappa^2 + \mu_i^2}}, \quad (55)$$

$$A_a(\kappa) = \frac{K}{\pi H}B_3\left[\ln\frac{\sqrt{k_m^2 + \mu_i^2} + \sqrt{k_m^2 - \kappa^2}}{\sqrt{k_m^2 + \mu_i^2} - \sqrt{k_m^2 - \kappa^2}} + 2\frac{k_m^2 + \mu_i^2}{\kappa^2 + \mu_i^2}\left(1 - \frac{\sqrt{k_m^2 - \kappa^2}}{\sqrt{k_m^2 + \mu_i^2}}\right)\right]. \quad (56)$$

Similarly, in the Stokes−Wilson scattering region ($\kappa \ge k_m$), we obtain:

$$r_{\text{diff}}(\kappa) = MB_{S-W}(\kappa), \quad (57)$$

$$B_{S-W}(\kappa) = \frac{Kk_m^2}{2(\kappa^2 + \mu_i^2)^{3/2}}\left(B_1 + \frac{3}{2}a_\kappa B_2\right). \quad (58)$$

The interference absorption coefficient describes the extinction effect for diffusely scattered waves and is given by the relationship:

$$\mu_i(\Delta\theta, \Delta\theta') = \frac{\mu_0}{2\gamma_0} \frac{b+1}{2} \frac{E}{|g|} [r_i(z) + r_i(z')], \qquad (59)$$

where the notation was used:

$$r_i(z) = \sqrt{(\sqrt{u^2 + v^2} - u)}/2,$$

$$u = (z^2 - g^2)E^{-2} + \tilde{\kappa}^2 - 1, \; v = 2(zgE^{-2} - p),$$

$$z = \frac{\Delta\theta \sin(2\theta_B)}{C|\chi_{rH}|}\sqrt{b}, \; \; z' = \frac{(\Delta\theta' - \Delta\theta)\sin(2\theta_B)}{C|\chi_{rH}|}\sqrt{b},$$

$$g = -\frac{|\chi_{i0}|}{|\chi_{rH}|}\frac{\sqrt{b}+1/\sqrt{b}}{2C}, \; \; p = \frac{\mathrm{Re}(\chi_{rH})\mathrm{Re}(\chi_{iH}) + \mathrm{Im}(\chi_{rH})\mathrm{Im}(\chi_{iH})}{|\chi_{rH}|^2}, \; \; \tilde{\kappa} = \frac{|\chi_{iH}|}{|\chi_{i0}|}.$$

The interference absorption coefficient μ_i plays in Eqs. (53) to (58) a role of the cut-off parameter and removes the non-physical divergence at $\kappa \rightarrow 0$. This coefficient also allows for the correct description of the diffuse component contribution to TCD diffraction profiles in the region of coherent peak, where this contribution is rapidly decreased approximately by an order of magnitude.

If several types of microdefects are present within the crystal simultaneously, without mutual correlation, the Eqs. (53) and (57) should be simply replaced by the sum of corresponding expressions for each type of defects.

The above consideration allows to describe the complex diffraction patterns measured by TCD from single crystals with complicated defect structures and, particularly, to explain the asymmetrical behaviour of coherent peaks on TCD profiles due to taking into account the influence of microdefects and disturbed layers in monochromator, analyser, and sample crystals.

3.2. Differential-Integral Method

The diffraction profiles measured by TCD from the investigated crystal, which contains homogeneously distributed microdefects, as functions of deviation angle $\Delta\theta'$ of the analyser crystal at fixed deviation angle $\Delta\theta$ of the investigated sample are usually consisting of three peaks. Namely, there are observed the main peak at $\Delta\theta'_M = (1 + b_S)\Delta\theta$, pseudo-peak at $\Delta\theta'_S = \Delta\theta$ and diffuse peak at $\Delta\theta'_D = 2\Delta\theta\sin^2\theta_B$. A form of the pseudo-peak is determined by the reflection coefficient of the monochromator, whereas the forms of main and diffuse peaks are de-

termined by the coherent and diffuse components of the reflection coefficient of the investigated sample, respectively. These peaks are well separated at sufficiently large deviations $\Delta\theta$ on the sample, which are significantly greater than the width W of its total reflection range.

The integrated intensities of coherent (main) and diffuse peaks depend only on the angular deviation $\Delta\theta$ of the investigated crystal and are connected unambiguously with the coherent and diffuse components of the reflection coefficient of this crystal, the sum of which is measured by the double-crystal diffractometer (DCD) with widely open detector window. These connections can be established easily by integrating the expressions (46) and (48) over $\Delta\theta'$ in the vicinity of points $\Delta\theta'_{M}$ and $\Delta\theta'_{D}$. If the condition $\left|\Delta\theta\right| \gg W$ is fulfilled and the peaks are well separated, the corresponding integrals are factorized simply [16]:

$$I_{M}(\Delta\theta) \approx I_0 R_{iM} R_{iA} R_{coh}(\Delta\theta), \qquad (60)$$

$$I_{D}(\Delta\theta) \approx I_0 R_{iM} R_{iA} R_{diff}(\Delta\theta). \qquad (61)$$

In Eqs. (60) and (61), the next notation was used:

$$R_{coh}(\Delta\theta) = \left|r(\Delta\theta)\right|^2, \qquad (62)$$

$$R_{diff}(\Delta\theta) = \int d(\Delta\theta') \, r_{diff}(\boldsymbol{\kappa}) = \int\limits_{K'=K} R_{D}(\mathbf{k}) d\Omega_{\mathbf{K}'}, \qquad (63)$$

where $d\Omega_{\mathbf{K}'}$ is a solid angle in $\mathbf{K}'$ direction, and $R_{coh}(\Delta\theta)$ and $R_{diff}(\Delta\theta)$ describe the coherent and diffuse components of rocking curve measured by DCD [22], respectively. The value of the error made at such factorization is of the order of $W^2/\left|\Delta\theta\right|^2$.

The ratio of the integrated intensities of coherent and diffuse peaks $Q(\Delta\theta) = I_{D}(\Delta\theta) / I_{M}(\Delta\theta)$, as can be seen from Eqs. (46) and (48), will not depend on the instrumental factors of TCD. After accounting for the summation over X-ray polarizations, this ratio takes the form:

$$Q(\Delta\theta) = \frac{R_{diff}^{\sigma}(\Delta\theta) + \rho R_{diff}^{\pi}(\Delta\theta)}{R_{diff}^{\sigma}(\Delta\theta) + \rho R_{diff}^{\pi}(\Delta\theta)}, \qquad (64)$$

where $\rho = \left|\cos(2\theta_B^M)\cos(2\theta_B^A)\right|$, θ_B^M and θ_B^A are the Bragg angles of monochromator and analyser, respectively. When obtaining the formula (64), it was supposed that the approximate relationships hold $R_{iM}^{\pi} \approx \left|\cos(2\theta_B^M)\right| R_{iM}^{\sigma}$ and $R_{iA}^{\pi} \approx \left|\cos(2\theta_B^A)\right| R_{iA}^{\sigma}$.

The diffuse component of the reflection coefficient of the crystal with homogeneously distributed defects after the integration over output angles can be represented as follows [22, 28]:

$$R_{diff}(\Delta\theta) \cong F_{dyn}(\Delta\theta) \frac{\mu_{ds}(\Delta\theta)}{2\gamma_0\mu(\Delta\theta)}, \qquad (65)$$

where the dependence of the interference absorption coefficient μ_i on exit angles $\Delta\theta'$ was neglected because its influence is smoothed due to integration, and thus μ_i in Eq. (59) can be replaced by its limiting value at $|\Delta\theta'| \gg W$:

$$\mu_i \rightarrow \mu(\Delta\theta) = \frac{\mu_0}{2\gamma_0}\frac{1+b}{2}\Big[1 + Er_i(z)\,/\,|g|\Big]. \tag{66}$$

The absorption coefficient due to diffuse scattering from microdefects in Eq. (65) is described by the expression:

$$\mu_{ds}(k_0) = cC^2 E^2 m_0 J(k_0), \tag{67}$$

$$J(k_0) = \begin{cases} J_H(k_0) + J_{H-SW}(k_0) + \tilde{J}_H(k_0), \text{ at } |k_0| \le k_m, \\ J_{SW}(k_0), \text{ at } |k_0| \ge k_m; \end{cases} \tag{68}$$

here, $k_0 = K\Delta\theta\sin(2\theta_B)$. The angular dependence of the 'integral' diffuse scattering intensity in the Huang scattering region is described by symmetric (J_H) and antisymmetric ($\tilde{J}_H$) components in Eq. (68) as follows:

$$J_H(k_0) = b_2 \ln\frac{k_m^2 + \mu^2}{k_0^2 + \mu^2} + (b_3 k_0^2 + b_4\mu^2)\left(\frac{1}{k_m^2 + \mu^2} - \frac{1}{k_0^2 + \mu^2}\right), \tag{69}$$

$$J_{H-SW}(k_0) = b_2 - \frac{1}{2}\frac{b_3 k_0^2 + b_4\mu^2}{k_m^2 + \mu^2}, \tag{70}$$

$$J_{SW}(k_0) = \frac{k_m^2 + \mu^2}{k_0^2 + \mu^2}\left(b_2 - \frac{1}{2}\frac{b_3 k_0^2 + b_4\mu^2}{k_0^2 + \mu^2}\right), \tag{71}$$

$$\tilde{J}_H(k_0) = b_1(\sqrt{k_m^2 + \mu^2} - \sqrt{k_0^2 + \mu^2}). \tag{72}$$

The coefficients b_i $(i = \overline{1,4})$ in Eqs. (69)–(72) are connected with characteristics of microdefects by relations:

$$b_1 = \frac{4L_H\sqrt{B_2}}{cH}, \quad b_2 = B_1 + (B_2\cos^2\theta_B)/2, \tag{73}$$

$$b_3 = B_2((\cos^2\theta_B)/2 - \sin^2\theta_B), \quad b_4 = B_2((\cos^2\theta_B)/2 - \cos^2\psi).$$

It should be remarked that the absorption coefficient due to diffuse scattering in the above equations is the sum of corresponding coefficients in the case of several randomly distributed defect types. Similar superposition law is supposed to be valid for the exponent of static Krivoglaz–Debye–Waller factor as well. The last is also immediately connected with defect characteristics by following relationships for

dislocation loops and spherical clusters, respectively [24, 33]:

$$L_H \cong \frac{1}{2} n_L R_L^3 (Hb)^{3/2},$$ (74)

$$L_H \cong \begin{cases} 0.525 n_C \upsilon_C n_0 \eta^4, \ \eta \leq 1.9, \\ n_C \upsilon_C n_0 \eta^3, \ \eta > 1.9, \end{cases}$$ (75)

$$\eta = \sqrt{\Gamma |\varepsilon| H R_C}, \ \ n_0 = \frac{4\pi R_C^3}{3\upsilon_c},$$

where $n_L = c_L / \upsilon_c$ and $n_C = c_C / \upsilon_c$ are number densities of dislocation loops and spherical clusters, respectively.

The above-written formulas establish analytical relations between coherent and diffuse components of the reflection coefficients measured by high-resolution double- and triple-crystal diffractometers from imperfect crystals in Bragg diffraction geometry, on the one hand, and statistical characteristics of defects, on the other hand.

Thus, a closed set of the analytical relationships is formed which can provide the self-consistent dynamical description and quantitative analysis of the rocking curves and diffraction profiles measured by the high-resolution double- and triple-crystal diffractometers, respectively, from imperfect crystals containing randomly distributed defects of several types to determine more reliably their structural characteristics.

3.3. Separation of Coherent and Diffuse Components of Integrated Diffraction Intensity

The investigation of crystal imperfections by using measurements of the integrated X-ray diffraction intensities has a number of advantages such as rapidity, high sensitivity, and simple data treatment. The multicrystal arrangements provide the unique possibility to separate the coherent and diffuse components of the integrated diffraction intensity from imperfect crystals containing randomly distributed defects and thus to enhance the sensitivity to defect characteristics due to their direct connections with the integrated diffuse component [34, 35].

In particular, the experimental TCD setup has been proposed for direct measurements of the integrated diffuse component at Laue diffraction geometry on the investigated crystal [36]. In this setup (Fig. 3, *a*), the mutual disorientation of monochromator and sample crystals has been used to screen the X-rays exciting the coherent component of scattering intensity in the sample under investigation. In another proposed TCD setup (Fig. 3, *b*), the thin analyser crystal set in the exact Bragg reflection geometry was used as screen for the coherent component of diffraction intensity from the sample whereas the diffuse com-
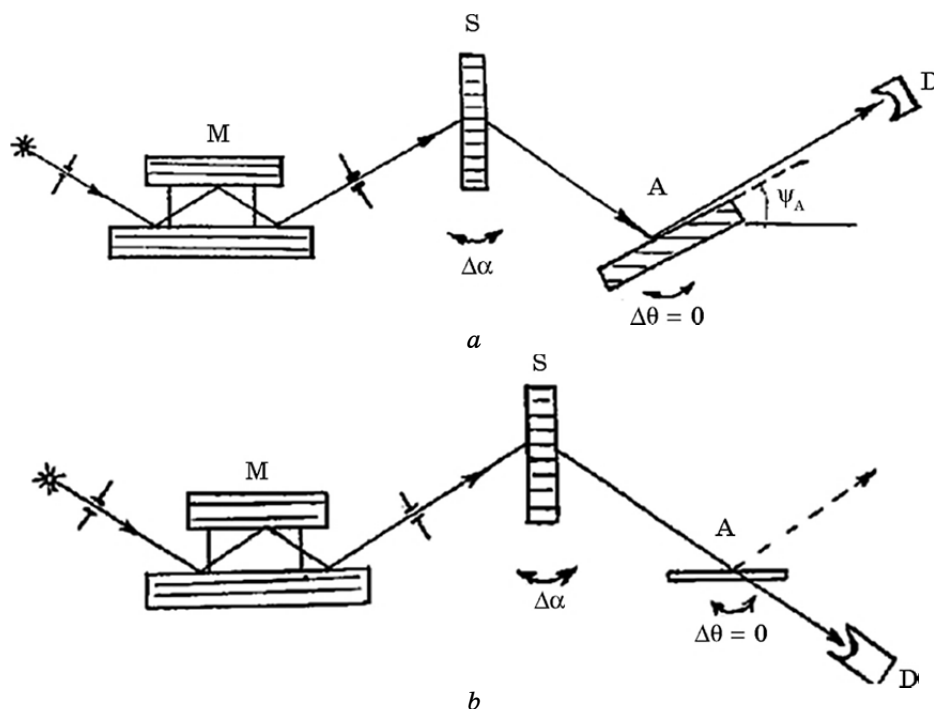
Fig. 3. TCD schemes used to measure separately the coherent (*a*) and diffuse (*b*) components of total integrated reflecting power at Laue X-ray diffraction geometry on the investigated crystal (S) [36, 37].

ponent was transmitted to the detector [37].

4. CHARACTERIZATION OF DEFECTS AND STRAINS IN SINGLE CRYSTALS BY USING TCD

4.1. Defect Structure of Annealed Czochralski-Grown Silicon Crystal

4.1.1. Annealing at High Temperatures

A) Anneal at 1100°C during 40 min and 5.5 h. The two investigated samples of 1 mm thickness with (100) surface orientation were cut from Czochralski-grown silicon (Cz-Si) ingot of *n*-type conductivity (10 Ω·cm) with initial oxygen concentration about 10^{18} cm^{-3}. The samples were annealed in wet oxygen atmosphere at 1100°C during 40 min and 5.5 h. As known, the enhanced oxygen precipitation is occurred in the silicon samples at such conditions of the thermal treatment.

Measurements of diffraction profiles (see Fig. 4) were carried out by using the non-dispersive TCD scheme with flat monochromator and

analyser silicon crystals (see Fig. 1) and the samples were set in the symmetrical Bragg diffraction geometry [15]. The measured profiles showed the high and narrow diffuse peaks located at $\Delta\theta' = 0$ and evidenced for the existence of strong diffuse scattering from large oxygen precipitates. Moreover, the analysis of these profiles led to the necessity for accounting the influence of the loose precipitate interface created by emitted silicon interstitials and like that described recently in the experimental investigation of oxygen precipitation in highly boron-doped Cz-Si [38].

In the case of clusters with loose interface, the diffuse component of the differential crystal reflectivity (40) can be modified according to the model proposed by Krivoglaz as follows [15, 24]:

$$R_{\mathrm{D}}(\mathbf{k}) \sim F(\mathbf{q})\left|s(\mathbf{k})\right|^2, \tag{76}$$

where the Fourier component of the ellipsoidal cluster form-factor is described by the expression:

$$s(\mathbf{k}) = n_0 v_{\mathrm{c}} \exp\left(-\frac{1}{2} \sum_{i=x,y,z} k_i^2 R_i^2\right), \tag{77}$$

$$n_0 = (2\pi)^{3/2} R_x R_y R_z / v_{\mathrm{c}},$$

and R_i are the lengths of ellipsoid semi-principal axes. After integrating Eq. (76) over vertical divergence, the diffuse component of the diffraction profiles for imperfect crystals with randomly distributed ellipsoidal microdefects having the loose interface can be approximately described by the following expression:

$$I_{\mathrm{diff}}(\Delta\theta, \ \Delta\theta') \sim r_{\mathrm{diff}}(k_x, k_z) \exp(-k_x^2 R_x^2 - k_z^2 R_z^2), \tag{78}$$
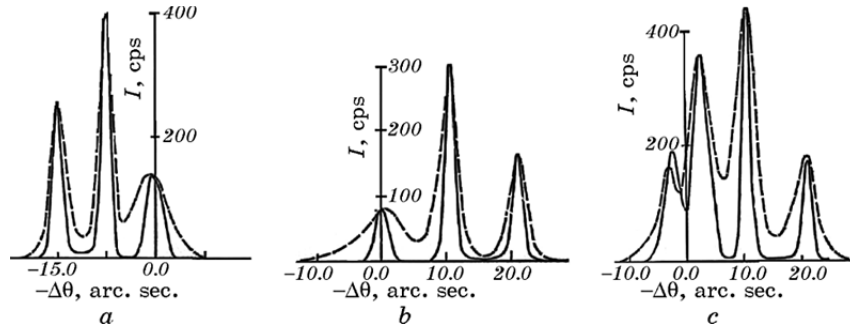

Fig. 4. Measured and calculated diffraction profiles (dashed and solid lines, respectively) measured by TCD from Cz-Si samples annealed at 1100°C during 40 min (*a*, *b*) and 5.5 h (*c*) for Si(004) reflection of MoK_α-radiation [15].

where $r_{\mathrm{diff}}(k_x, k_z)$ is given by Eq. (53).

The fit of the measured diffraction profiles was performed to achieve coincidence of heights and positions of main, pseudo-, and diffuse peaks at measured and calculated curves by varying oxygen precipitate radii, concentration, and the static Krivoglaz–Debye–Waller factor. The treatment of the diffraction profiles measured from the sample annealed during 40 min (Fig. 4, *a* and *b*) has given the following values: $R_x = R_y \cong 13$ nm and $R_z \cong 650$ nm, with small differences in $c(A_C/v_c)^2 = 1.4 \cdot 10^{-6}$ and $E \cong 0.7$ for the profile shown in Fig. 4, *a* and $c(A_C/v_c)^2 = 2.2 \cdot 10^{-6}$ and $E \cong 0.6$ for the profile shown in Fig. 4, *b*. The treatment of the diffraction profiles measured from the sample an-
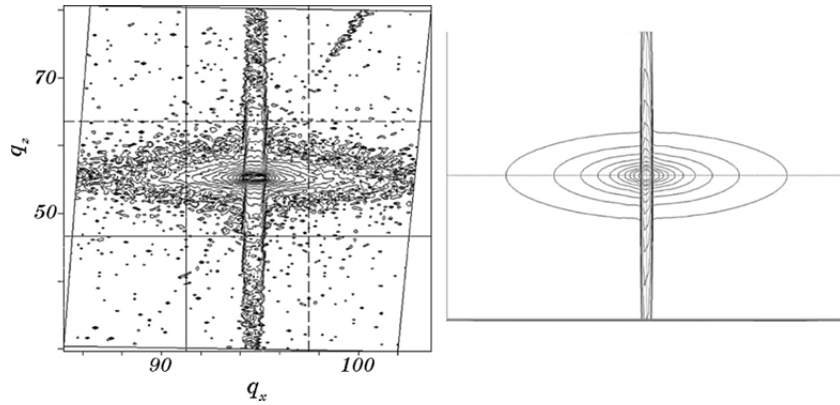

Fig. 5. Measured (left) and calculated (right) reciprocal space maps for the Cz-Si sample annealed at 1150°C during 50 h, Si(111) reflection, CuK_α-radiation [39].
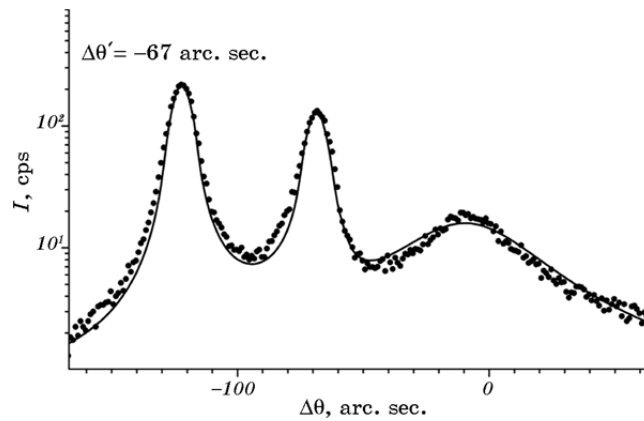

Fig. 6. Measured and calculated diffraction profile (markers and solid line, respectively) from Cz-Si sample annealed at 1150°C during 50 h, Si(111) reflection, CuK_α-radiation [39].

nealed during 5.5 h (Fig. 4, *c*) has given the following values: $R_x = R_y \cong$ $\cong 260$ nm, $R_z \cong 1300$ nm, $c(A_C/v_c)^2 = 2.5 \cdot 10^{-6}$, and $E \cong 0.4$. The remained visible discrepancies between measured and calculated diffraction profiles can be caused by the existing spread of oxygen precipitate radii and ignoring instrumental factors.

B) Anneal at 1150°C during 50 h. The investigated sample was cut from Cz-Si ingot and annealed in argon atmosphere at 1150°C during 50 h. The measurements of reciprocal space maps (Fig. 5) were performed by using the diffractometer PANanalytical X`Pert Pro MRD XL at symmetrical Si(111) reflection on the sample in Bragg diffraction geometry of characteristic $CuK_{\alpha1}$-radiation (see Fig. 2).

Additionally, the measurements of diffraction profiles (Fig. 6) were performed in the non-dispersive scheme of the home-made TCD with a higher resolution at symmetrical Si(111) reflections in Bragg diffraction geometry of characteristic $CuK_{\alpha1}$-radiation on all three flat crystals [39]. To describe defect structure in the investigated Cz-Si sample, the model was used supposing the presence of two microdefect types (see, *e.g.*, Ref. [40]), namely, the spherical amorphous oxygen precipitates SiO_2 (radius R_P, thickness h_P, and number density n_P) and circular dislocation loops with Burgers vector $\mathbf{b} = <110>/2$ (radius R_L and number density n_L).

As can be seen from Table 1, the characterization results obtained from the reciprocal space map coincide sufficiently well for predominant type of defects (large dislocation loops) with those obtained from the set of diffraction profiles measured by the home-made TCD one of which is shown in Fig. 6. Some discrepancy in the concentration can be explained by the presence of smaller dislocation loops and oxygen precipitates, which also give contributions to the diffraction pattern. The detailed quantitative characterization of small oxygen precipitates and dislocation loops was possible due to additional using the set of diffraction profiles measured by the home-made TCD (see also Ref. [41]).

It should be emphasized that the exclusively important factor for the reliable determination of characteristics of these defects was the use of the generalized dynamical theory, which permits determining simultaneously a set of defect characteristics due to the self-consistent

TABLE 1. Radii and number densities of spherical oxygen precipitates and circular dislocation loops in Cz-Si sample annealed at 1150°C during 50 h [39].

Data type	R_P, nm	n_P, cm^{-3}	R_L, μm	n_L, cm^{-3}
Profile	10 ± 1	$(1.0 \pm 0.1) \cdot 10^{13}$	0.05 ± 0.005 0.3 ± 0.03 5.0 ± 0.3	$(8.0 \pm 2) \cdot 10^{11}$ $(9.0 \pm 3) \cdot 10^{9}$ $(4 \pm 0.5) \cdot 10^{7}$
Map	–	–	4.3 ± 0.6	$(1.9 \pm 1) \cdot 10^{8}$

consideration of both diffuse and coherent components of diffraction patterns. The availability of the explicit analytical expressions for diffuse scattering intensity, which take the anisotropy of displacement fields around dislocation loops with discrete orientations into account [39], was also important.

C) Anneal at 1160°C during 50 h. The investigated Si single crystal was cut from Cz-Si ingot with p-type conductivity ($\rho = 10$ Ω·cm) and initial oxygen concentration about $1.1 \cdot 10^{18}$ cm^{-3}. The sample of 478 μm thickness was annealed in argon atmosphere at 1160°C during 50 h with subsequent heat hardening in air. The measurements of diffraction profiles (Fig. 7) were performed in the non-dispersive TCD scheme with symmetrical reflections Si(111) in Bragg diffraction geometry of characteristic Cu$K_{\alpha 1}$-radiation on all three flat crystals (see Fig. 1) [16].

The set of TCD profiles was measured at fixed angular positions of the sample under investigation versus angular deviation of the analyser crystal. As can be seen form an example in Fig. 7, the presence of diffuse scattering from defects in monochromator crystal leads to a rapid increase or decrease of the pseudo-peak height in comparison with that of main peak in dependence on the sign of the sample deviation. Such asymmetrical behaviour can be explained only by accounting for the contribution of the antisymmetric part of diffuse scattering intensity from microdefects in monochromator crystal [18].

The angular dependence of the ratio of diffuse to coherent integrated peak intensities calculated from the set of measured TCD profiles is shown in Fig. 8. The treatment of this dependence was performed for the defect model of spherical amorphous new phase SiO$_2$ particles by using Eq. **(64)**. The fit shows a good agreement between experimental observations and theoretical calculations at following values of oxygen precipitate characteristics: $R_\mathrm{C} = (0.94 \pm 0.10)$ μm and $n_\mathrm{C} = (1.2 \pm 0.1) \cdot 10^6$ cm^{-3}.

D) Anneal at 1180°C during 6 h. The silicon single crystal was cut from the Cz-Si ingot perpendicularly to (111) growth axis. The sample of about 500 μm thickness was annealed at 1180°C during 6 h. Measurements of thickness dependences of the separated coherent and diffuse components of the total integrated reflecting power (Fig. 9) were carried out by the inclination method at Laue diffraction geometry on the investigated crystal in both TCD (Fig. 3) and DCD optical schemes with symmetrical Si(220) reflections of characteristic Mo$K_{\alpha 1}$-radiation on all three crystals [36, 37].

In the optical TCD scheme used to separate coherent component of total integrated reflecting power (Fig. 3, *a*), the asymmetrically cut Si analyser crystal was chosen to strongly decrease the receiving aperture for the X-ray beam diffracted from the sample.

In the optical TCD scheme used to separate diffuse component of total integrated reflecting power (Fig. 3, *b*), the thin Si analyser crystal was set in the exact reflecting Bragg diffraction geometry to reflect
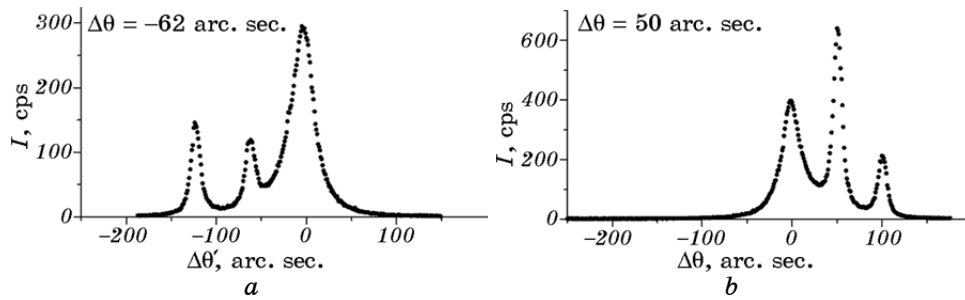
Fig. 7. Diffraction profiles measured by TCD for the symmetrical Si(111) reflection of Cu$K_{\alpha 1}$-radiation from the Cz-Si sample annealed at 1160°C during 50 h [16] at the negative (*a*) and positive (*b*) angles of sample deviation.

the coherent component and to provide the transmission with low attenuation for X-ray beam diffracted from the sample outside the total reflection range.

The fit of the measured thickness dependence of the total integrated reflecting power evidenced its low sensitivity to defect characteristics of the investigated nearly perfect silicon crystal. Namely, the following values of the absorption coefficient due to diffuse scattering, normalized to the photoelectric absorption coefficient, $\mu_{ds}^{0} / \mu_{0} = 0.3 \pm 0.5$, and the exponent of static Krivoglaz–Debye–Waller factor $L_{220} =$
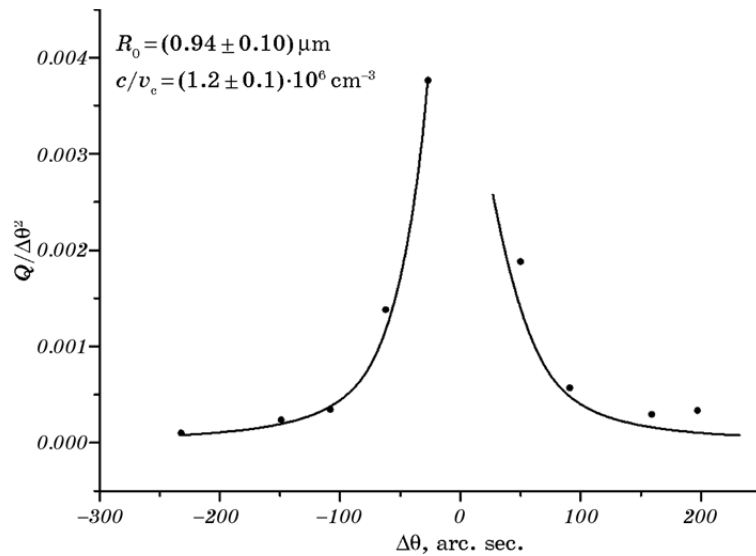

Fig. 8. Angular dependence of the ratio of diffuse to coherent integrated peak intensities calculated from measured TCD profiles (points—experiment, solid line—theory) [16].
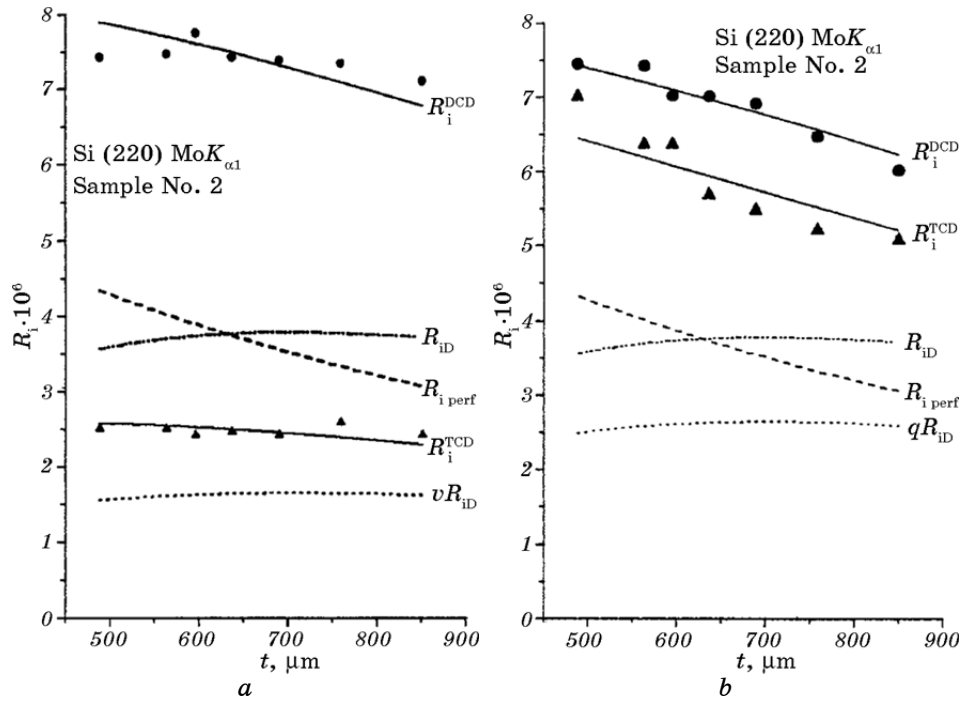
Fig. 9. Thickness dependences of the separated coherent and diffuse components of total integrated reflecting power measured by the inclination method using optical TCD schemes shown: (*a*)—in Fig. 3, *a* and (*b*)—in Fig. 3, *b* corresponding to Bragg and Laue diffraction geometries for the investigated silicon crystal, respectively (markers—experiment; solid, dot, dashed, and dot-dashed lines—theory) [36, 37].

$= 0.005 \pm 0.001$ were found. However, the additional fit of the measured thickness dependence of the separated coherent component of total integrated reflecting power (see Figs. 3, *a* and 9, *a*) at fixed value of $L_{220} = 0.005$ allowed the determination of the absorption coefficient due to diffuse scattering with sufficiently high precision, namely, $\mu^0_{ds} / \mu_0 = 0.23 \pm 0.02$.

The thickness dependences of the total integrated reflecting power and its diffuse component separated by using the optical TCD scheme shown in Fig. 3, *b* are represented in Fig. 9, *b*. The fit of the separated diffuse component at fixed value of $L_{220} = 0.005$ allowed determining the value of absorption coefficient due to diffuse scattering, $\mu^0_{ds} / \mu_0 = 0.25 \pm 0.02$, which is very close to that determined by the previous method.

Thus, both the optical TCD schemes used to separate measured coherent and diffuse components of the total integrated reflecting power allow for increasing, in comparison with the conventional inclination

method, the precision of determination of the second important defect characteristics, namely, the absorption coefficient due to diffuse scattering, additionally to static Krivoglaz–Debye–Waller factor.

4.1.2. Annealing at Low Temperature

The investigated Cz-Si crystal of 480 μm thickness has been cut from the central part of 10 cm wafer with (111) surface orientation perpendicular to growth axis. The sample of p-type conductivity with the resistance of 10.5 Ω·cm, which contained $1.1 \cdot 10^{18}$ cm^{-3} and less than $1.0 \cdot 10^{17}$ cm^{-3} of oxygen and carbon atoms, respectively, was annealed at 750°C during 50 h.

Measurements of TCD profiles (Fig. 10, a) were carried out in Bragg diffraction geometry near reciprocal lattice point (111) in the non-dispersive scheme $(n, -n, n)$ by automated home-made TCD with flat monochromator and analyser crystals (see Fig. 1). Also, the rocking curves were measured in the mode of DCD with widely open detector window [42].

In the model used to describe defect structure in the investigated Cz-Si sample, the presence of two types of microdefects was supposed, namely, the disk-shaped amorphous oxygen precipitates SiO_2 (radius R_P, thickness h_P, and number density n_P) and chaotically oriented circular dislocation loops of interstitial type with Burgers vector $\mathbf{b} = <110>/2$ (radius R_L and number density n_L) (see, $e.g.$, [20]). The contribution from thermal diffuse scattering was simulated by the diffuse scattering from spherical clusters with the radius equal to the covalent one of silicon atom $R_P = 1.17$ Å and concentration $n_P = 5 \cdot 10^{22}$ cm^{-3}, $i.e.$, concentration of silicon atoms. The value of strain at
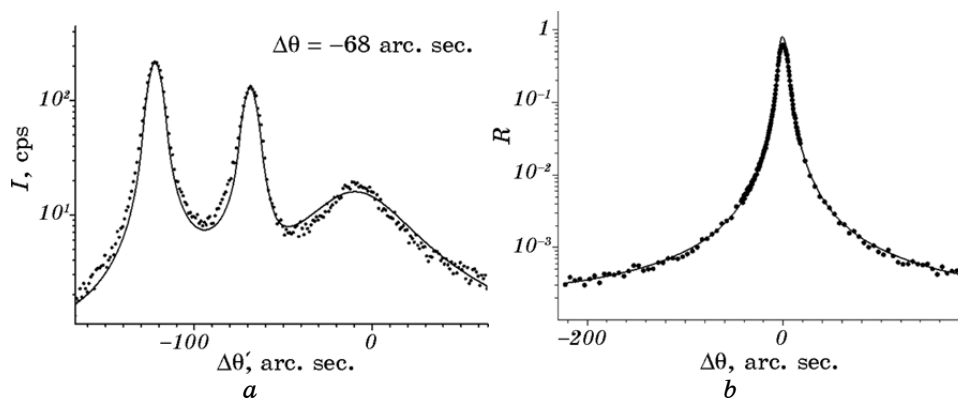

Fig. 10. Fitted TCD profile (a) and rocking curve (b) for Si(111) reflection of $CuK_{\alpha 1}$-radiation from Cz-Si sample annealed at 750°C during 50 h [42].

TABLE 2. Characteristics of disk-shaped oxygen precipitates and circular dislocation loops in Cz-Si crystal annealed at 750°C during 50 h [42].

R_P, nm	h_P, nm	n_P, cm^{-3}	ε	R_L, μm	n_L, cm^{-3}
10 ± 1	5.0 ± 0.5	$(3.0 \pm 0.3) \cdot 10^{13}$	0.0242	0.045 ± 0.003	$(5.0 \pm 1.5) \cdot 10^{11}$
				0.25 ± 0.03	$(5.8 \pm 1.6) \cdot 10^{9}$
				5.0 ± 0.3	$(4 \pm 1) \cdot 10^{7}$

such 'cluster' boundary $\varepsilon \cong 0.25$ has been found by fitting and corresponds well with the mean-square deviation of vibrating Si atoms. The defect characteristics given in Table 2 have been determined by the self-consistent fitting the measured rocking curve and TCD profiles.

The successful treatment of diffraction profiles measured by TCD and DCD was possible due to their different sensitivities to microdefects of different types and sizes. In particular, the contributions of diffuse scattering intensity from small microdefects, point defects, and thermal vibrations to TCD profiles are significantly smaller in magnitude as compared to those from large microdefects. On the other hand, these contributions are comparable on DCD profiles due to the additional integration of diffuse scattering intensity over vertical divergence. More important, however, was the use of the common theoretical approach to the description of diffraction profiles measured by TCD and DCD, namely, the generalized dynamical theory of X-ray scattering in real single crystals [10–17]. Thus, the most complete characterization of the defect structure in the investigated sample can be achieved after combined measurements by TCD and high-resolution DCD with joint treatment of experimental data by using this theory.
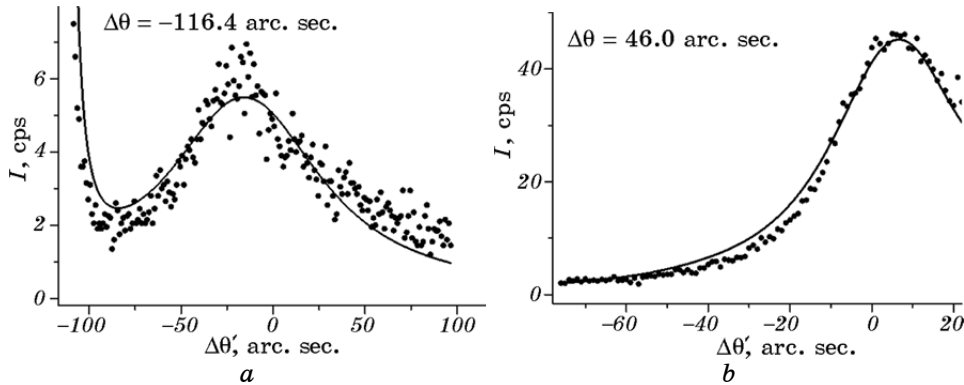

Fig. 11. Measured and calculated TCD diffraction profiles (markers and solid line, respectively) versus analyser deviation angle ($\Delta\theta'$) at fixed values of deviation angle ($\Delta\theta$) of the investigated Cz-Si sample annealed at 750°C during 50 h, Si(111) reflection, CuK_α-radiation [19].

TABLE 3. Characteristics of spherical oxygen precipitates and circular dislocation loops in Cz-Si crystal annealed at 750°C during 50 h [19].

R_P, nm	n_P, cm^{-3}	R_L, μm	n_L, cm^{-3}
		0.05	$8 \cdot 10^{11}$
0.01	$1 \cdot 10^{13}$	0.3	$9 \cdot 10^{9}$
		5.0	$4 \cdot 10^{7}$

In Ref. [42], such approach has allowed to determine not only the characteristics of small and large microdefects in the crystal bulk but also the strain in subsurface layer, which is caused by the so called 'mirror image forces' from all the defects in crystal bulk. This strain was described by the exponential law $\varepsilon_\perp(z) = \varepsilon_\perp^0 \exp(-z/t_0)$, where z is the depth, and the parameters have been determined to be equal $t_0 = 7$ nm and $\varepsilon_\perp^0 = 10^{-4}$.

It is of interest to compare the determined defect characteristics with those obtained for the same sample two years ago in a similar research [19], where the measurements of TCD profiles (Fig. 11) were carried out also in Bragg diffraction geometry by the home-made TCD. The model of defect structure of the investigated Cz-Si sample, which was used to fit the measured TCD diffraction profiles and rocking curves, was different only in that the presence of the spherical instead of disk-shaped amorphous oxygen precipitates SiO_2 was supposed. The defect characteristics given in Table 3 have been determined by the self-consistent fitting the measured rocking curves and TCD profiles.

As can be seen by comparing the defect characterization data from Tables 2 and 3, the average volume of oxygen precipitates remained unchanged within the fit error after two-year conservation at the room temperature. Moreover, the characteristics of large dislocation loops are constant. At the same time, the small dislocation loops have been partially dissolved after two-year ageing by emitting nearly half of their silicon interstitials.

4.2. Defect Structure of the Silicon Crystal Grown by Floating-Zone Method

The investigated sample has been cut from the central part of the oxygen-free silicon single-crystalline plate grown by the floating-zone method (FZ-Si). The conventional X-ray topography and scanning electron microscopy have not revealed any defects in the sample.

The model of defect structure in the investigated FZ-Si sample, which was chosen to describe the measured diffraction profiles [17], was based on results of direct observations of FZ-Si crystals by the

transmission electron microscopy [43–46]. This model includes three types of defects, namely, circular dislocation loops of interstitial type with the Burgers vector <110>/2, disc-shaped precipitates of unknown nature, and point defects. The later ones give a small contribution to rocking curve tails in the measured $\Delta\theta$ range, being comparable to that of thermal diffuse scattering, but affect appreciably the diffraction pattern through the corresponding significant addition to the exponent of the static Krivoglaz–Debye–Waller factor.

Monochromator and analyser crystals used in TCD were identical to the investigated sample, *i.e.*, they have been cut from the central part of the same FZ-Si plate. TCD measurements were carried out in non-dispersive scheme (n, $-n$, n) with symmetric (111) reflections in Bragg diffraction geometry on all three crystals by using $CuK_{\alpha 1}$-radiation from the conventional X-ray tube (see Fig. 1). The TCD diffraction profiles (Fig. 12) were measured at fixed sample deviation $\Delta\theta$ by rotating analyser crystal ($\Delta\theta'$) with using the step motor. The very low heights of diffuse peaks as compared to coherent ones indicate immediately the high perfection of the crystal under investigation.

The rocking curves for symmetrical Bragg (111) and (333) reflections of $CuK_{\alpha 1}$-radiation were measured by the high-resolution DCD with widely open detector window (Fig. 13). The dispersive (m, m, $-n$) scheme was used in DCD with one-fold symmetrical Ge(333) reflections on both monochromator crystals.

The fit of diffuse peaks on TCD profiles (Fig. 12) and DCD rocking curves (Fig. 13) was performed supposing the same defect model. It should be emphasized also that the separate measurement of diffuse
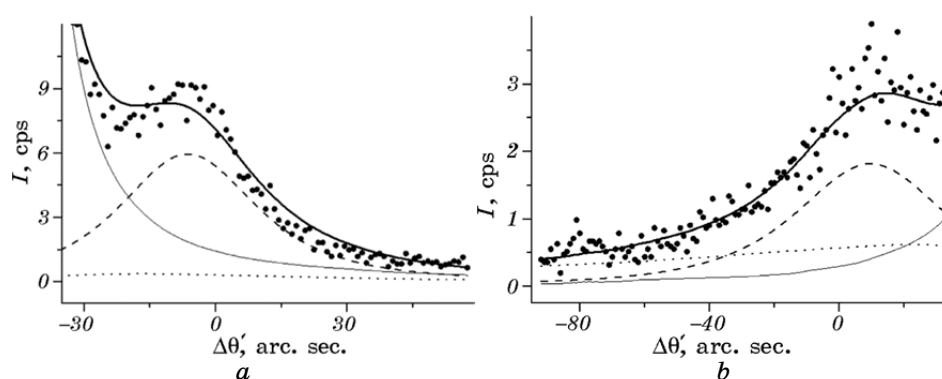

Fig. 12. Diffuse peaks on the diffraction profiles measured by TCD at sample deviations $\Delta\theta = -49$ (*a*) and 73 arc sec (*b*), FZ-Si(111) reflection of $CuK_{\alpha 1}$-radiation. The calculated diffraction profile is constituted of coherent and diffuse components (thick solid, thin solid, and dash-dotted lines, respectively), the last one is the sum of diffuse scattering intensities from dislocation loops and precipitates (dashed and dotted lines, respectively) [17].
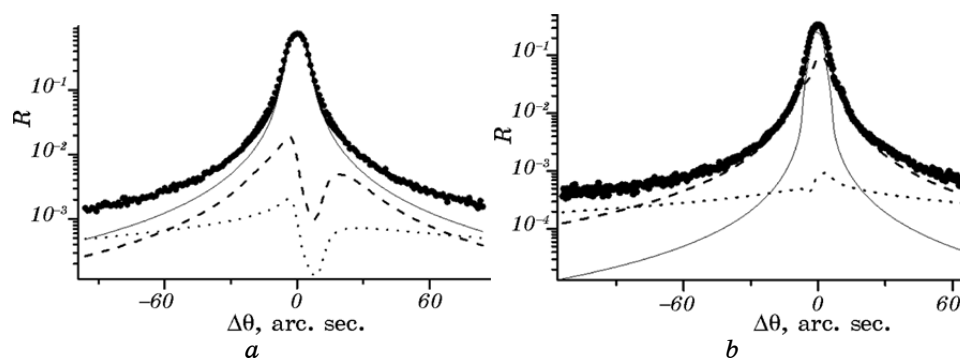
Fig. 13. Rocking curves measured for FZ-Si 111 (*a*) and 333 (*b*) reflections, Cu$K_{\alpha 1}$-radiation. The calculated total rocking curves and their coherent components are shown by thick and thin solid lines, respectively, and diffuse scattering intensity contributions from dislocation loops, precipitates, and point defects are shown by dashed, dotted, and dash-dotted lines, respectively [17].

scattering intensity by TCD has allowed the determination of the interstitial nature of the precipitates, which give the noticeable antisymmetric part to the observed diffuse scattering intensity. It was important also to verify the obtained results, which follow from the analysis of the diffuse scattering intensity superimposed in DCD measurements with the coherent scattering intensity, by the more direct observation of diffuse scattering intensity profiles measured by TCD separately from coherent ones.

The determined characteristics of microdefects (radii R_L and R_P as well as number densities n_L and n_P of dislocation loops and disc-shaped precipitates, respectively) are listed in Table 4. The values of these characteristics, which have been obtained from different diffraction experiments, are sufficiently close one to other. The sizes of both type microdefects are in surprisingly good correspondence with those found in the direct observations of another FZ-Si crystal [43]. The discrepancies of number densities and size values can originate from the smallness of crystal volumes probed in the transmission electron microscopy and, obviously, from different growth conditions.

The characteristics of microdefects in the investigated FZ-Si sample have been repeatedly determined from the diffraction profiles (**Fig. 14**) and reciprocal space map (**Fig. 15**) measured by TCD five years later (see Table 5). As can be seen from Tables 4 and 5, the characteristics of dislocation loops in the FZ-Si sample have been only little changed after five year conservation at the room temperature. However, the measurement and analysis of the reciprocal space map enables for the refinement of their average increased radius. At the same time, the average number of silicon interstitials in dislocation loops remained

TABLE 4. Microdefect characteristics determined from the diffraction profiles measured by DCD and TCD for FZ-Si sample [17].

Method	hkl	R_L, μm	n_L, cm^{-3}	R_P, nm	n_P, cm^{-3}
DCD	111	1.0	$2.9 \cdot 10^8$	50	$1.8 \cdot 10^{11}$
	333	0.8	$1.8 \cdot 10^8$	50	$3.2 \cdot 10^{11}$
TCD	111	0.7	$4.5 \cdot 10^8$	50	$1.0 \cdot 10^{11}$

TABLE 5. Characteristics of circular dislocation loops in FZ-Si sample obtained by fitting total TCD profile and reciprocal space map [39].

Data type	hkl	R_L, μm	n_L, cm^{-3}
Profile	111	1.15 ± 0.1	$(3.5 \pm 1) \cdot 10^8$
Map	111	2.1 ± 0.5	$(7.3 \pm 3) \cdot 10^7$

nearly unchanged due to the decreased concentration of these dislocation loops.

4.3. Defect Structure of the Cz-Si Crystal after High-Energy Electron Irradiation

The investigated Cz-Si samples of (111) surface orientation and thicknesses $t \cong 4.26$ mm have been irradiated with doses 1.8 and 3.6 kGy (Nos. 1A and 1B, respectively) of high-energy electrons (18 MeV). The as-grown sample No. 1 was used as etalon for the comparison with the irradiated samples.

Reciprocal space maps of the samples under investigation were measured by PANalytical X`Pert Pro MRD XL diffractometer (see Fig. 2) for the symmetrical Si(333) reflection of characteristic $CuK_{\alpha 1}$-radiation [47, 48]. Additionally, the rocking curves for Si(333) reflection were measured in the ω-scanning mode by using the TCD with removed analyser crystal.

The thorough comparative analysis of the measured reciprocal space maps (Fig. 16), their cross-sections (Fig. 17), and rocking curves (Fig. 18) was performed to achieve their mutual consistence on the base of a common set of defect characteristics. For this sake, the appropriate model of the defect structure was chosen which is typical for both as grown and annealed Cz-Si samples and consists of two types of randomly distributed microdefects, namely, oxygen precipitates and interstitial dislocation loops [40].

The fit of the measured diffraction profiles and reciprocal space maps was carried out at neglecting the contributions from the thermal diffuse scattering and diffuse scattering from point defects as being
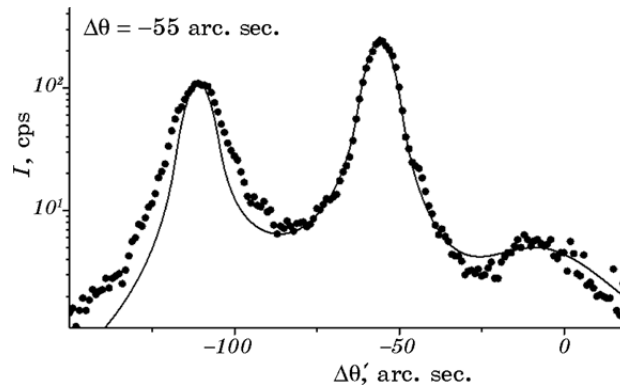
Fig. 14. Measured and calculated TCD diffraction profile (markers and solid line, respectively) versus analyser deviation angle $\Delta\theta'$ at fixed deviation angle of the investigated FZ-Si sample $\Delta\theta = -55$ arc sec, Si(111) reflection, CuK_{α_1}-radiation [39].
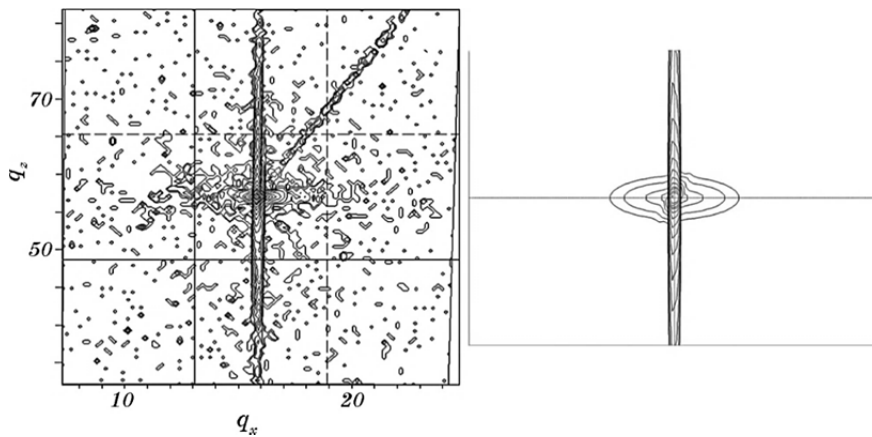

Fig. 15. Measured (left) and calculated (right) reciprocal space maps for the FZ-Si sample, Si(111) reflection, CuK_α-radiation [39].

relatively small in the considered reciprocal space region [28].

In the analysis first of all, the fact was established that it was impossible to describe any of the experimental reciprocal space maps having nearly oval shapes by using only spherical oxygen precipitates because the typical shape of the diffuse scattering intensity distribution for these defects is the 'double droplet'. Therefore, the attempts were undertaken to fit jointly the diffraction profiles and rocking curves supposing the simultaneous presence of both types of microdefects, namely, spherical oxygen precipitates and circular interstitial dislocation loops. However, the account for the presence of both type defects with single sizes does
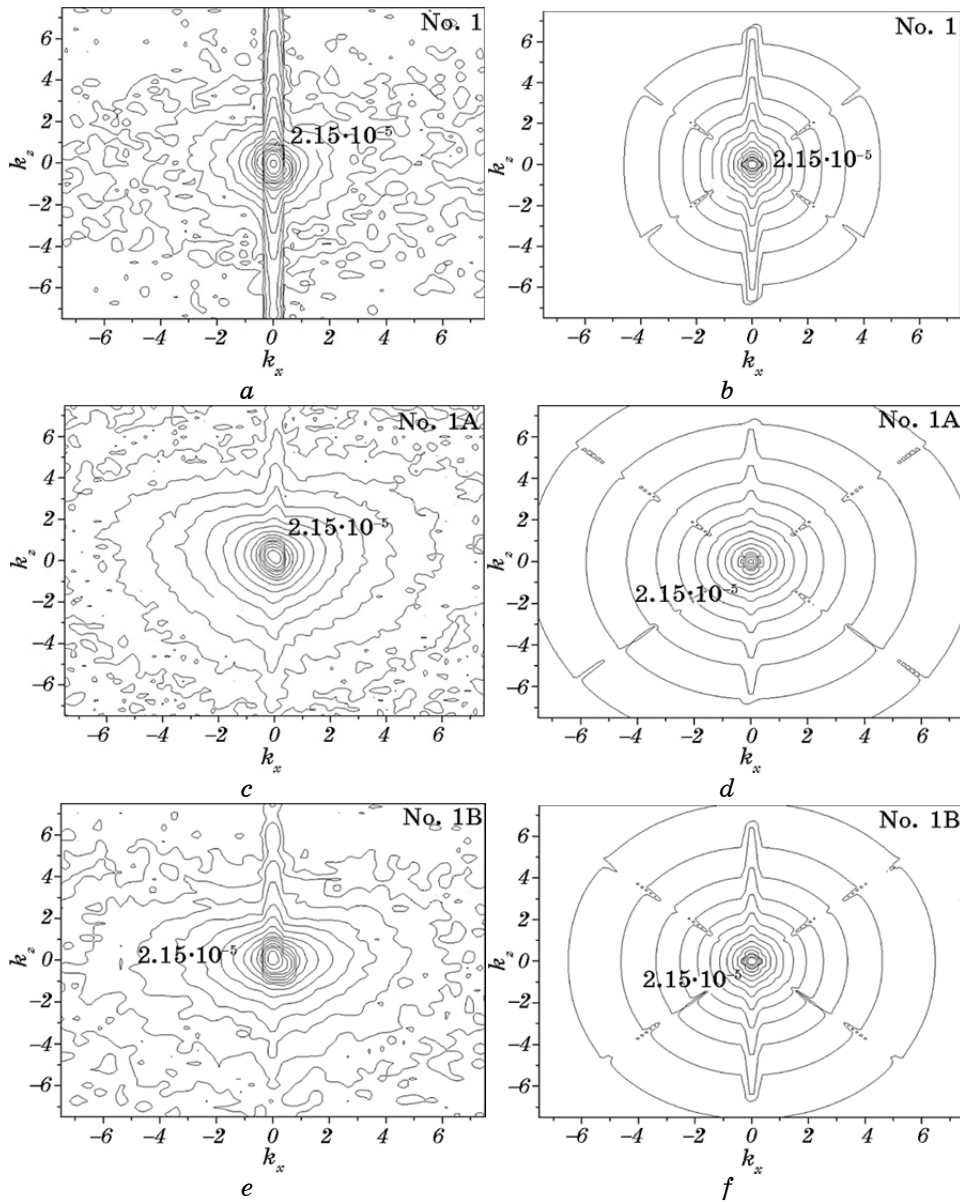
Fig. 16. Measured (*a*, *c*, *e*) and calculated (*b*, *d*, *f*) reciprocal space maps of the as grown (No. 1—*a*, *b*) and electron-irradiated (No. 1A—*c*, *d*, and No. 1B—*e*, *f*) Cz-Si samples; (333) reflection, Cu$K_{\alpha 1}$-radiation. The intensities of neighbouring equal intensity lines differ by a factor of $10^{1/3}$, the quantities k_x and k_z are given in units of the reciprocal lattice parameter $d^{-1} \cdot 10^{-4}$ [48].

not provide sufficiently good fits of all the diffraction patterns.

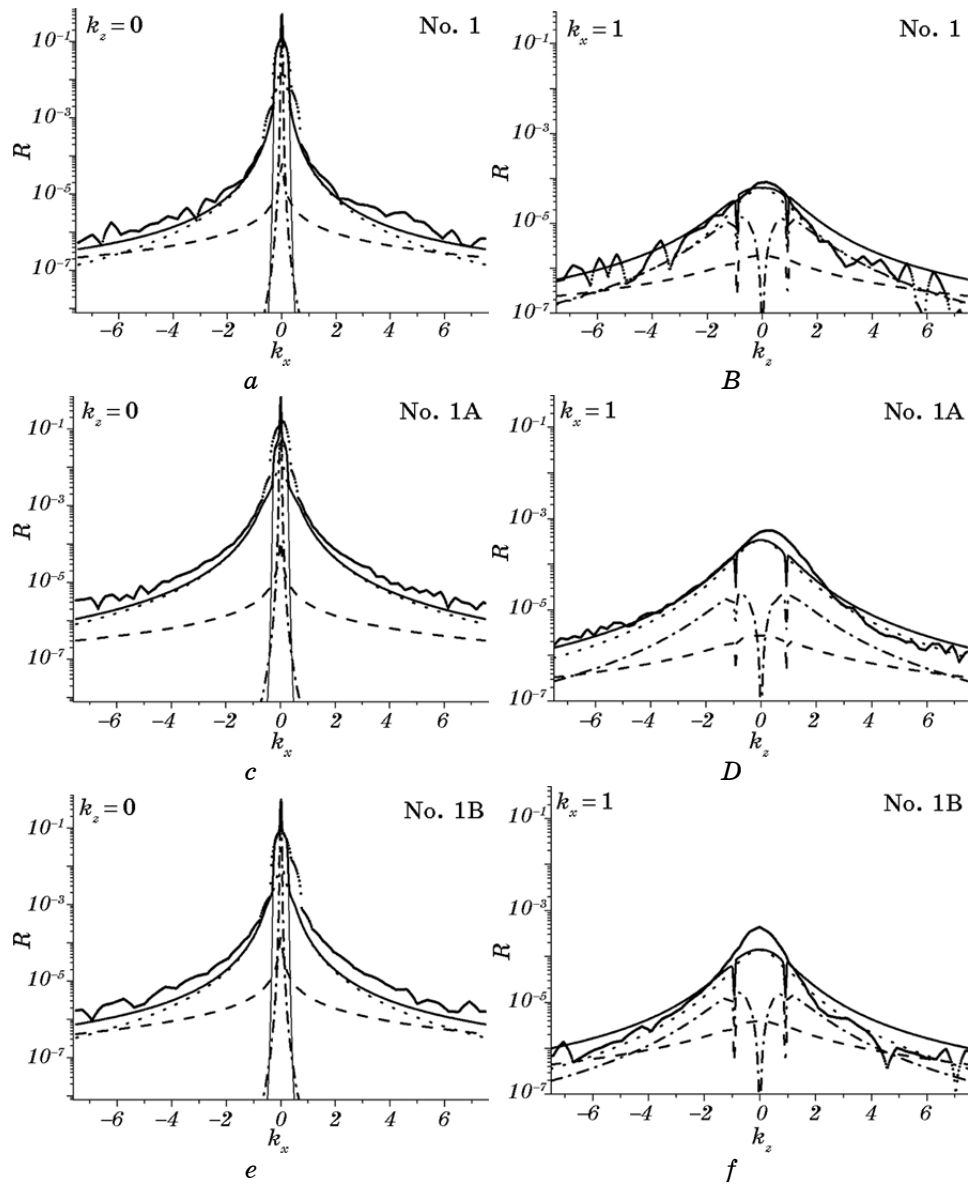To obtain the acceptable fit, the assumption on the presence of dislo-

Fig. 17. Transverse (*a*, *c*, *e*) and longitudinal (*b*, *d*, *f*) cross-sections of the measured reciprocal space maps from Fig. 11 and their calculated profiles (markers and thick solid line, respectively), the last consist of coherent and diffuse components with contributions from small and large dislocation loops, and oxygen precipitates (thin solid, dashed, dotted, and dot-dashed lines, respectively) [48].
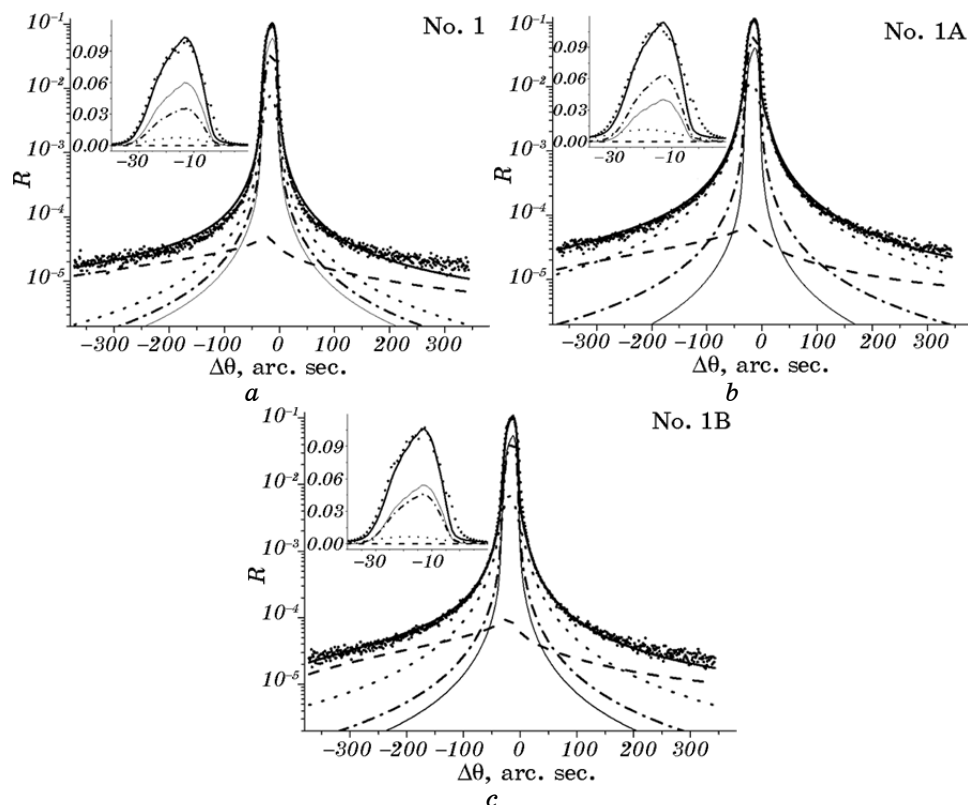
Fig. 18. Experimental and theoretical rocking curves (markers and thick lines) for the as-grown (*a*) and electron-irradiated Cz-Si samples Nos. 1A (*b*) and 1B (*c*); (333) reflection of Cu$K_{\alpha 1}$-radiation. Other lines are explained in caption of Fig. 17. Central parts of the rocking curves are shown in the insets [48].

cation loops with two different sizes, namely, large and small ones, was necessary to be made (see the defect characteristics in Table 6).

Thus, the simultaneous description of the rocking curves and reciprocal space maps measured from both as-grown and irradiated Cz-Si samples is possible only if contributions from defects with at least three effective radii are considered. On the other hand, the appropriate shape of the equal intensity lines on all the maps can only be ensured by the predominant contribution of diffuse scattering from dislocation loops. The analysis of these maps demonstrated that the shape of equal intensity lines is typical for the case of circular dislocation loops with ⟨111⟩ orientations of Burgers vectors [39]. The radii of these (large) dislocation loops R_L were estimated using the measured reciprocal space maps and their cross sections (Figs. 16 and 17). For the irradiated samples, they turned out to be two fold less than for the as-grown

TABLE 6. Characteristics of dislocation loops (radius R_L and concentration n_L) and oxygen precipitates (R_P and n_P) in the as-grown (No. 1) and electron-irradiated (Nos. 1A and 1B) Cz-Si samples [48].

Sample No.	R_L, μm	n_L, cm^{-3}	R_P, μm	n_P, cm^{-3}
1	0.002 0.15	$1.15 \cdot 10^{16}$ $3.3 \cdot 10^{11}$	1.0	$7.5 \cdot 10^{6}$
1A	0.003 0.065	$5.0 \cdot 10^{15}$ $1.0 \cdot 10^{13}$	1.0	$1.25 \cdot 10^{7}$
1B	0.003 0.07	$5.0 \cdot 10^{15}$ $3.5 \cdot 10^{12}$	1.0	$9.0 \cdot 10^{6}$

crystal. The concentration n_L of these loops in the irradiated samples proved to be significantly (by an order of magnitude and more) larger as compared to the concentration in the as-grown sample (see Table 6).

The estimate for radii of large spherical oxygen precipitates $R_P \cong 1$ μm in all samples was obtained simultaneously with that for large loops. Their concentration n_P in the irradiated samples significantly increased as compared with as-grown one.

Final values of the characteristics of large dislocation loops and oxygen precipitates were obtained after introducing small dislocation loops into the combined treatment. These loops with radii of several nanometres give significant contributions at far tails of the rocking curves for all studied samples but their contributions are negligible in the TCD diffraction profiles (compare Figs. 17 and 18). As can be seen from the Table 6, the concentrations of small dislocation loops in the irradiated samples are approximately two fold smaller than in the as-grown crystal.

The obtained results have been interpreted as follows. Under irradiation with high energy electrons the defect structure in the bulk of the silicon crystal is transformed due to the influence of two factors, namely, the creation of radiation defects, first of all, vacancies and interstitial silicon atoms, and the increase of crystal temperature (to approximately 1000°C at the chosen irradiation parameters) which enhances diffusion processes. As can be seen from the results of diagnostics (Table 6), both these factors have significant influence on the decomposition processes of supersaturated solid solution of oxygen in silicon and results in considerable changes of the growth defect characteristics in both irradiated silicon samples as compared to the as-grown crystal.

Thus, the obtained results demonstrate the possibility of increasing the unambiguity of the quantitative characterization of complex defect structures in imperfect single crystals owing to the joint treatment of reciprocal space maps and rocking curves.

5. RESUME AND CONCLUSIONS

The basic principles of the dynamical theory of X-ray diffraction by crystals with chaotically distributed microdefects are described. Based on this theory, the analytical expressions for the coherent and diffuse scattering intensities measured by TCD from crystals containing microdefects of several types have been derived. Peculiarities of TCD measurements, which are connected with the presence of additional contributions in reflection coefficients of all the crystals of X-ray optical scheme due to both strained subsurface layers and diffuse scattering from defects in these crystals, have been taken into account as well.

The developed theoretical model for the description of total TCD profiles and reciprocal lattice maps has allowed for performing the quantitative characterization of complicated defect structures in imperfect single crystals at qualitatively new level of uniqueness and reliability. Besides, the analysis of total diffraction profiles measured by TCD with flat monochromator and analyser crystals has provided the possibility of reliable establishment of the role of diffuse scattering from the monochromator crystal in the formation of coherent peaks on TCD profiles. In particular, the account for the influence of these factors has allowed for giving the correct explanation of the asymmetrical behaviour of main and pseudo-peaks on TCD profiles.

It is necessary to emphasize the especially important role of the joint processing reciprocal space maps and rocking curves for reliable quantitative determination of the microdefect characteristics with a wide spread in their effective sizes. The analysis of reciprocal space maps is the simplest way to unambiguously establish the dominant type of microdefects that make the main contribution to the measured differential diffuse scattering intensity distributions and to determine the approximate characteristics of these defects. At the same time, owing to integration of the diffuse scattering intensity over the Ewald sphere, rocking curves are more sensitive to small size defects as compared to reciprocal space maps in which the contribution from small defects is almost negligible.

The developed self-consistent dynamical theoretical model for the description of total TCD diffraction profiles, reciprocal space maps, and rocking curves has allowed for achieving the qualitatively new level of uniqueness and reliability of defect characterization by using their joint treatment. In particular, the quantitative characterization of the complicated microdefect structures created in various silicon crystals grown by the Czochralski and floating-zone methods have been determined by analytical treatment of the measured TCD profiles, rocking curves, and reciprocal space maps.

REFERENCES

1. P. Eisenberger, N. G. Alexanropoulos, and P. M. Platzmann, *Phys. Rev. Lett.*, **28**, No. 23: 1519 (1972).
2. B. C. Larson and W. G. Schmatz, *Phys. Rev. B*, **10**, No. 6: 2307 (1974).
3. A. Iida and K. Kohra, *phys. status solidi (a)*, **51**, No. 2: 533 (1979).
4. A. Iida, *phys. status solidi (a)*, **54**, No. 2: 701 (1979).
5. A. M. Afanas'ev, M. V. Koval'chuk, E. F. Lobanovich, R. M. Imamov, P. A. Aleksandrov, and M. K. Melkonyan, *Kristallografiya*, **26**, Iss. 1: 28 (1981) (in Russian).
6. E. K. Kov'ev, V. V. Ratnikov, and L. M. Sorokin, *Fizika Tverdogo Tela*, **23**, No. 6: 1626 (1981) (in Russian).
7. P. Zaumseil and U. Winter, *phys. status solidi (a)*, **70**, No. 2: 497 (1982).
8. P. Zaumseil and U. Winter, *phys. status solidi (a)*, **73**, No. 2: 455 (1982).
9. A. A. Lomov, P. Zaumseil, and U. Winter, *Acta Crystallogr. A*, **41**, No. 3: 223 (1985).
10. R. N. Kyutt, A. A. Sitnikova, and L. M. Sorokin, *Fizika Tverdogo Tela*, **27**, No. 3: 673 (1985) (in Russian).
11. V. Holý and J. Kuběna, *phys. status solidi (b)*, **170**, Iss. 1: 9 (1992).
12. L. A. Charniy, A. N. Morozov, V. T. Bublik, K. D. Scherbachev, I. V. Stepantsova, and V. M. Kaganer, *J. Cryst. Growth*, **118**: 163 (1992).
13. V. Holý, U. Pietch, and T. Baumbach, *High-Resolution X-Ray Scattering from Thin Films and Multilayers* (Berlin–Heideiberg: Springer: 1998).
14. P. F. Fewster, *X-Ray Scattering from Semiconductors* (London: Imperial College Press: 2000).
15. V. B. Molodkin, S. I. Olikhovskii, M. E. Osinovskii, V. V. Kochelab, A. Yu. Kazimirov, M. V. Koval'chuk, and F. N. Chukhovskiy, *Metallofizika*, **6**, No. 3: 7 (1984) (in Russian).
16. V. B. Molodkin, V. V. Nemoshkalenko, S. I. Olikhovskii, E. N. Kislovskii, O. V. Reshetnyk, T. P. Vladimirova, V. P. Krivitsky, V. F. Machulin, I. V. Prokopenko, G. E. Ice, and B. C. Larson, *Metallofiz. Noveishie Tekhnol.*, **20**, No. 11: 29 (1998).
17. V. B. Molodkin, M. Ando, E. N. Kislovskii, S. I. Olikhovskii, T. P. Vladimirova, O. V. Reshetnyk, E. G. Len, E. A. Evgrafova, and E. V. Pervak, *Metallofiz. Noveishie Tekhnol.*, **24**, No. 4: 541 (2002).
18. S. I. Olikhovskii, V. B. Molodkin, E. M. Kislovskii, O. V. Reshetnyk, T. P. Vladimirova, E. G. Len, G. E. Ice, R. I. Barabash, R. Köhler, and D. O. Grigoriev, *Metallofiz. Noveishie Tekhnol.*, **27**, No. 7: 949 (2005).
19. S. I. Olikhovskii, V. B. Molodkin, E. M. Kislovskii, O. V. Reshetnyk, T. P. Vladimirova, G. E. Ice, R. I. Barabash, R. Köhler, and D. O. Grigoriev, *Metallofiz. Noveishie Tekhnol.*, **27**, No. 9: 1251 (2005).
20. V. B. Molodkin, S. I. Olikhovskii, and M. E. Osinovskii, *Metallofizika*, **5**, No. 1: 3 (1983) (in Russian).
21. V. B. Molodkin, S. I. Olikhovskii, E. N. Kislovskii, E. G. Len, and E. V. Pervak, *phys. status solidi (b)*, **227**: 429 (2001).
22. S. I. Olikhovskii, V. B. Molodkin, E. N. Kislovskii, E. G. Len, and E. V. Pervak, *phys. status solidi (b)*, **231**: 199 (2002).
23. V. S. Wang and R. J. Matyi, *J. Appl. Phys.*, **72**, Iss. 11: 5158 (1992).
24. M. A. Krivoglaz, *X-Ray and Neutron Scattering in Nonideal Crystals* (Berlin:

Springer: 1996).
25. P. H. Dederichs, *Phys. Rev. B*, **4**: 1041 (1971).
26. R. Bloch, D. Bahr, J. Olde, L. Brügemann, and W. Press, *Phys. Rev. B*, **42**: 5093 (1990).
27. T. P. Vladimirova, R. F. Seredenko, V. B. Molodkin, S. I. Olikhovskii, and E. N. Kislovskii, *Metallofiz. Noveishie Tekhnol.*, **29**, No. 6: 711 (2007) (in Ukrainian).
28. V. B. Molodkin, S. I. Olikhovskii, E. N. Kislovskii, T. P. Vladimirova, E. S. Skakunova, R. F. Seredenko, and B. V. Sheludchenko, *Phys. Rev. B*, **78**, No. 22: 224109 (2008).
29. V. P. Klad'ko, L. I. Datsenko, J. Bak-Misiuk, V. F. Machulin, I. V. Prokopenko, V. B. Molodkin, S. I. Olikhovskii, and Z. V. Maksimenko, *J. Phys. D: Applied Physics*, **34**, No. 10A: A87 (2001).
30. E. N. Kislovskii, O. V. Reshetnyk, T. P. Vladimirova, V. B. Molodkin, S. I. Olikhovskii, B. V. Sheludchenko, R. F. Seredenko, and E. S. Skakunova, *Metallofiz. Noveishie Tekhnol.*, **29**, No. 5: 701 (2007) (in Ukrainian).
31. A. P. Shpak, V. B. Molodkin, S. I. Olikhovskii, Ye. M. Kislovskii, O. V. Reshetnyk, T. P. Vladimirova, E. G. Len, A. I. Nizkova, V. M. Venger, and S. V. Dmitriev, *phys. status solidi (b)*, **204**, No. 8: 2651 (2007).
32. V. B. Molodkin, S. I. Olikhovskii, E. S. Skakunova, E. G. Len, E. N. Kislovskii, O. V. Reshetnyk, T. P. Vladimirova, V. V. Lizunov, L. N. Skapa, S. V. Lizunova, E. V. Fuzik, N. G. Tolmachev, B. K. Ostafiychuk, V. M. Pylypiv, and O. Z. Garpul'. *Metallofiz. Noveishie Tekhnol.*, **37**, No. 8: 1017 (2015).
33. E. S. Skakunova, *Metallofiz. Noveishie Tekhnol.*, **37**, No. 4: 555 (2015).
34. J. Chikawa, Y. Asaeda, and I. Fujimoto, *J. Appl. Phys.*, **41**: 1922 (1970).
35. V. Holý, and J. Kuběna, *phys. status solidi (b)*, **141**, No. 1: 35 (1987).
36. V. V. Nemoshkalenko, V. B. Molodkin, E. N. Kislovskii, S. I. Olikhovskii, T. A. Grishchenko, M. T. Kogut, and E. V. Pervak, *Metallofiz. Noveishie Tekhnol.*, **22**, No. 2: 42 (2000) (in Russian).
37. V. G. Bar'yahtar, V. V. Nemoshkalenko, V. B. Molodkin, A. P. Shpak, D. Chikava, K. Kohra, R. N. Kyutt, S. I. Olikhovskii, A. I. Nizkova, T. A. Grishchenko, E. N. Kislovskii, M. T. Kogut, and M. V. Koval'chuk, *Metallofizika*, **15**, No. 12: 72 (1993) (in Russian).
38. C. Bergmann, A. Gröschel, J. Will, and A. Magerl, *J. Appl. Phys.*, **118**: 015707 (2015).
39. V. B. Molodkin, S. I. Olikhovskii, E. G. Len, E. N. Kislovskii, V. P. Kladko, O. V. Reshetnyk, T. P. Vladimirova, and B. V. Sheludchenko, *phys. status solidi (a)*, **206**, No. 8: 1761 (2009).
40. A. Borgesi, B. Pivac, A. Sasella, and A. Stella, *J. Appl. Phys.*, **77**: 4169 (1995).
41. V. B. Molodkin, S. I. Olikhovskii, Ye. M. Kyslovskyy, E. G. Len, O. V. Reshetnyk, T. P. Vladimirova, V. V. Lizunov, and S. V. Lizunova, *Semiconductor Physics, Quantum Electronics and Optoelectronics*, **13**, No. 4: 353 (2010).
42. A. P. Shpak, V. B. Molodkin, S. I. Olikhovskii, Ye. M. Kyslovskyy, O. V. Reshetnyk, T. P. Vladimirova, E. G. Len, A. I. Nizkova, V. M. Venger, and S. V. Dmitriev, *phys. status solidi (a)*, **204**, No. 8: 2651 (2007).
43. P. M. Petroff and A. J. R. de Kock, *J. Cryst. Growth*, **30**: 117 (1975).
44. H. Föll, V. Gösele, and B. O. Kolbesen, *J. Cryst. Growth*, **52**, No. 2: 907 (1981).
45. P. J. Roksnoer and M. M. B. van der Boom, *J. Cryst. Growth*, **53**, No. 3: 563

(1981).

46. P. J. Roksnoer, *J. Cryst. Growth*, **68**, No. 2: 596 (1984).

47. V. B. Molodkin, S. I. Olikhovskii, Ye. M. Kyslovskyy, T. P. Vladimirova, E. V. Kochelab, O. V. Reshetnyk, V. V. Dovganyuk, I. M. Fodchuk, T. V. Lytvynchuk, V. P. Klad'ko, and Z. Świątek, *phys. status solidi (a)*, **208**, No. 11: 2552 (2011).

48. E. N. Kislovskii, V. B. Molodkin, S. I. Olikhovskii, E. G. Len, B. V. Sheludchenko, S. V. Lizunova, T. P. Vladimirova, E. V. Kochelab, O. V. Reshetnik, V. V. Dovganyuk, I. M. Fodchuk, T. V. Litvinchuk, and V. P. Klad'ko, *J. Surface Investigation. X-Ray, Synchrotron and Neutron Techniques*, **7**, No. 3: 523 (2013).